Stony Brook University

Front Tracking and Application to Multi Phase Flow

A Dissertation Presented

by

Xingtao Liu

to

The Graduate School in Partial Fulfillment of the Requirements for the

Degree of

Doctor of Philosophy

in

Applied Mathematics and Statistics

Stony Brook University

August 2010

Stony Brook University

The Graduate School

Xingtao Liu

We, the dissertation committee for the above candidate for the Doctor of Philosophy
degree, hereby recommend acceptance of this dissertation.

James Glimm
Professor of Applied Mathematics and Statistics
Dissertation Advisor

Xiaolin Li
Professor of Applied Mathematics and Statistics
Chairman of Defense

Roman Samulyak
Associate Professor of Applied Mathematics and Statistics

James Davenport
Director of the Computational Science Center
Outside Member

This dissertation is accepted by the Graduate School.

Lawrence Martin
Dean of the Graduate School

Abstract of the Dissertation

Front Tracking and Application to Multi Phase Flow

by

Xingtao Liu

Doctor of Philosophy

in

Applied Mathematics and Statistics

Stony Brook University

2010

We mainly focus on the numerical simulation of primary breakup of a high speed jet using a front tracking method. Adaptive Mesh Refinement(AMR) method is used in the simulation, which can speed up the simulation extraordinarily. This work is the extension of earlier studies of Pro. Zhiliang Xu. We do a series of simulations to study systematically the parameters used in a cavitation model that he introduced. With the right choice of parameters, the Sauter mean diameter (SMD) of the droplets is in agreement with correlations based on experimental data. We also study the flow in the nozzle, to determine the level of cavitation within the nozzle and of the turbulence occurring at the nozzle exit. We find 2D-3D agreement for the mean velocity field and the occurrence of cavitation, but note some differences in the turbulence levels. To validate the capability of front tracking method in multiphase flow simulation, the primary Rayleigh Instability and Kelvin-Helmholtz Instability are also studied with

satisfactory results.

Table of Contents

List of Figures

List of Tables

Acknowledgements

I would like to thank my advisor, Prof. James Glimm, for the exciting topics suggested, for valuable discussions and for his guidance and continuous support. He shared his precious scientific experience and insights.

I also want to thank Prof. Xiaolin Li for his guidance and sharing his wisdom on conducting scientific research. His scientific vigor and dedication makes him a lifetime role model for me.

and Prof. Xiangming Jiao for the help when I worked on curvature problem.

and Prof. James Davenport and Prof. Roman Samulyak for being on my dissertation committee.

I would like to thank all my groupmates and friends, with whom I collaborated on most of my research works. Especially, I want to acknowledge Wurigen Bo who finished 3D jet simulations and gave me a lot of valuable suggestions.

Chapter 1

Introduction

Many methods have been proposed to evolve the fluid-gas interface; of these VOF, level set and front tracking methods are the most popular. A complete review is beyond the scope of this thesis. Readers are referred to the papers of Sethian [53], Scardovelli and Zaleski [50], Glimm *et al.* [13, 15], and Tryggvason *et al.* [58].

We use front tracking methods to solve the free surface flow. Front tracking has many advantages for the problems dominated by a geometrically complex and dynamically moving interface. It was used to simulate the Rayleigh-Taylor instability and gave impressive results [35, 36], including agreement with experiments in the overall growth rate as defined by the mixing growth rate parameter α. Since moving surfaces are tracked by marker particles, front tracking methods are able to model the interface accurately without any numerical diffusion across the interface, in contrast to capturing methods [11]. They also differ from marker particles methods in that particles are located only on the interface, rather than in a volume region near the interface. Geometrical information such as the surface normal and curvature is also easily computed in front tracking methods, as are surface related physical processes such as surface diffusion, surface tension, and surface mediated chemical reactions, because of the explicit representation of the interface by its own mesh.

The front tracking method is implemented in the code *FronTier*. In this chapter, we begin with a review of an interface tracking methods, i.e., the front tracking in *FronTier*.

1.1 The Front Tracking method in *FronTier*

The front tracking method is an adaptive computational method that provides sharp resolution of a wave front by tracking the interfaces between distinct materials. It represents interfaces explicitly as lower dimensional meshes moving through a rectangular grid. The states of fluids are located in the centers of each grid cell. Extensive work on front tracking method and its application in 2D space has been done by J. Glimm and his coworkers [17]. Great effort has been made for its extension to 3D space [14, 15]. We will give a brief introduction of the *FronTier* code in this section.

1.1.1 Equations of the system

In *FronTier*, the states in fluid are solved by conservation laws. The basic variables are density, momentum and total energy. The conservation laws for these variables can be written as

$$\mathbf{U}_t + \nabla \cdot \mathbf{F}(\mathbf{U}) = \mathbf{S} . \tag{1.1}$$

where

$$\mathbf{U} = \begin{pmatrix} \rho \\ \rho\mathbf{v} \\ \rho E \end{pmatrix} \quad \mathbf{F}(\mathbf{U}) = \begin{pmatrix} \rho\mathbf{v} \\ \rho\mathbf{v}\mathbf{v} + p\mathbf{I} \\ \rho E + p\mathbf{v} \end{pmatrix} , \tag{1.2}$$

are the conservative variables and their corresponding flux. ρ, the density, $\mathbf{v}$, the velocity, $E = e + \mathbf{v} \cdot \mathbf{v}/2$, the specific total energy, e, the specific internal energy. p,

the pressure, $\mathbf{I}$, an identity matrix. $\mathbf{S}$ represents the source terms for the equations which are used to model many physical effects such viscosity, gravity, mass diffusion and heat transfer. To close the system of equations, an equation of state $p = p(e, \rho)$ must be given. There can be moving surfaces inside the domain which represent physical waves such as contacts, shocks or the edges of rarefaction waves.

The equations (1.2) need to be written in a coordinate system. Far away from a surface, we write the equations (1.2) in a Cartesian coordinates system and seek a weak solution for the equations. On a surface, by assuming the surface is second order differentiable, we can find a local orthogonal coordinate system which has a normal direction $\mathbf{N}$ and tangential directions $\mathbf{T}$. The equations (1.2) can be rewritten in this coordinate system as

$$\mathbf{U}_t + \nabla_\mathbf{T} \cdot \mathbf{F}(\mathbf{U}) + \nabla_\mathbf{N} \cdot \mathbf{F}(\mathbf{U}) = \mathbf{S}_\mathbf{T} + \mathbf{S}_\mathbf{N} \ , \tag{1.3}$$

where the $\nabla_\mathbf{T}$ and $\nabla_\mathbf{N}$ represents the normal and the tangential components of the divergence operator ∇. $\mathbf{S}_\mathbf{N}$ and $\mathbf{S}_\mathbf{T}$ represent the normal and the tangential components of the source term $\mathbf{S}$.

1.1.2   Representation of the interface

In *FronTier*, a package called the interface library is used for the description and manipulation of interfaces. Details about this package can be found in [14–16]. We only give a brief summary of some basic terminology here.

The discontinuity in the numerical solution is described by an interface, which is discrete representation of a set of points, curves and surfaces. The boundaries of surfaces are curves, while boundaries of curves are called nodes. A curve is comprised of connected line segments. Each line segment in the curve is called a bond, which is

connector between two adjacent points. A surface is a connected oriented piecewise linear collection of triangles; each triangle contains 3 points. Both bonds and triangles are linking objects in the sense that they contains pointers to their neighbors. Each bond points to both the previous and following bonds that share its endpoints. Similarly, triangles share a common side with their neighbors and contain pointers to that neighbor's address. During front propagation, front intersections are produced due to wave interactions and require special treatment to resolve the interaction and untangle the interface. Figure 1.1 gives the representation of Interface in *FronTier*.
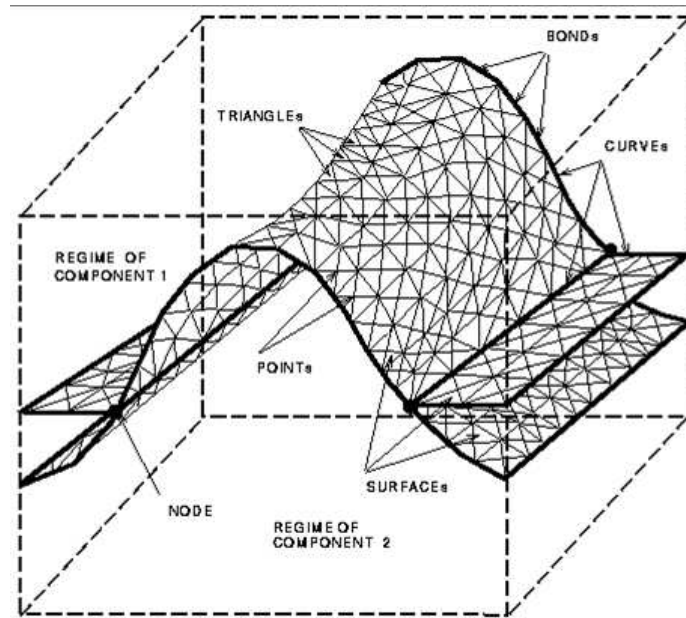
Figure 1.1: The representation of an interface in *FronTier*

For the 2D flows considered here, we assume the interface is represented by a set of curves (physical curve or non-physical), and each curve is composed by a set of bonds. There are no surface existing. For the 3D flows considered, we assume the interface is represented by a triangular mesh which is embedded in a rectangular domain. The interface divides the domain into a set of domains. The interface together with the

fixed boundaries of the rectangular domain form the boundaries of domains. Each domain is assigned by a component which is determined from the orientation of the surfaces/curves in the interface. Topological consistency requires that all components be identical for every surface/curves side bounding a given domain.

1.1.3 Front Tracking Method in *FronTier*

Front tracking method is implemented in *FronTier* by the following main steps

1. interface propagation.

    normal propagation

    interface reconstruction

    tangential propagation

2. interior states update.

In the interface propagation step, a local Riemann problem is solved with initial states interpolated from either side of the interface point. Then, a new position for the interface point is determined by using.

$$\mathbf{x}^{n+1} = \mathbf{x}^n + V\Delta t \mathbf{n}.$$ (1.4)

where $\mathbf{x}^n, \mathbf{x}^{n+1}$ are the old and the new positions of the point, V is the wave speed, $\mathbf{n}$ is the normal direction on the point and Δt is the time step size. The left and the right states on the interface are updated by the solution of the Riemann problem. Then the following equations on the tangent plane on each side of the interface are solved.

$$\mathbf{U}_t + \nabla_{\mathbf{T}} \cdot \mathbf{F}(\mathbf{U}) = \mathbf{S}_{\mathbf{T}} .$$ (1.5)

In the equations 1.5, we update the states on the interface without changing the positions of each point.

After all points in the interface are propagated, we get a new interface at a new time level. The interface may be badly distorted or have self-intersections. Methods are implemented in *FronTier* to resolve the topologically change and to optimize all triangles in the interface: grid free tracking, grid based tracking and locally grid based tracking. The details of the algorithm can be found in [8].

In the interpolation reconstruction step, the components in the cell center of all interior points are determined from the propagated interface. First, the crossings between the underlying Cartesian grid and the interface are calculated. Then, the components in cell centers are determined from these crossings. During this step, a ray casting algorithm in x, y and z directions is applied to find unphysical crossings. After this step, a component is uniquely assigned in each cell center.

In the interior state update step, a strang splitting method is applied and three 1D equations are solved consecutively. All the states on cell centers are updated by a finite difference scheme. If the stencil of the finite difference scheme does not cross any interface, the states in the stencil are given by the cell center values. Otherwise, a ghost cell method [18] is used to fill the states on the points on the other side of the interface. A new conservative front tracking scheme [34] has been implemented in *FronTier* recently, which eliminates the need for ghost cells.

1.2 Dissertation organization

The rest of this thesis is organized as follows: In Chapter 2, we present the detailed description of the liquid jet problem including the breakup mechanism and models. In Chapter 3 we explore the applications of our method in the numerical

study of diesel spray. In Chapter 4, we present a study of numerical simulations for the Kelvin-Helmholtz instability and Rayleigh instability.

Chapter 2

Introduction to high speed jets

2.1 Mechanism

The atomization of a high speed jet has been studied extensively in theory [32, 47, 48] and experiments [33, 38]. Primary jet breakup remains a challenging research topic due to its large range of spatial and temporal scales, and the complex flow regimes involved. Experimental observations are difficult because the droplets in the spray from the breakup obscure the spray interior and the liquid core. Numerical simulation appears to be a promising method to study the details of the breakup process of the liquid jet. However, the physical process of atomization poses difficulties for numerical algorithms. First, as the fuel has a much higher density than the ambient air, an accurate algorithm to deal with the interface between these two is required. Secondly, since the growth of perturbations on the interface is one of the important mechanisms in atomization [47], the algorithm should have small numerical diffusion so as not to suppress this process. Since one of the characteristics of atomization is topological change, such as breakup and merging of the interface, the algorithm must also resolve topological change robustly. During atomization, droplets whose diameter is much less than that of the nozzle are generated, and consequently, a high

resolution algorithm is required to resolve small droplets. Thirdly, liquid cavitation occurs inside the nozzle, mitigating pressure disturbances and influencing turbulence in the flow, as well as atomization.

Many methods have been proposed to evolve the fluid-gas interface; of these VOF, level set and front tracking methods are the most popular. A complete review is beyond the scope of this paper. Readers are referred to the papers of Sethian [53], Scardovelli and Zaleski [50], Glimm *et al.* [13, 15], and Tryggvason *et al.* [58].

We use front tracking methods to solve the free surface flow. Front tracking has many advantages for problems dominated by a geometrically complex and dynamically moving interface. It was used to simulate Rayleigh-Taylor instability and gave impressive results [30, 35, 36], including agreement with experiment in the overall growth rate as defined by the mixing growth parameter α. Since moving surfaces are tracked by marker particles, front tracking methods are able to model accurately an absence of mass diffusion across the interface for immiscible fluids and limited mass diffusion across a concentration isosurface for miscible fluids, in contrast to capturing methods [11]. They also differ from marker particle methods in that particles are located only on the interface, rather than in a volume region near the interface. Geometrical information, such as the surface normal and curvature, is easily computed in front tracking methods, as are surface related physical processes such as surface diffusion, surface tension, and surface mediated chemical reactions, due to the explicit representation of the interface by its own mesh. The front tracking method is implemented in the code *FronTier* [11].

The flow leading to liquid jet breakup is divided roughly into four parameter regions, according to the flow Reynolds and Weber numbers [27]. Here we are concerned with high speed jets, well within the third of these regimes, called the second wind driven regime. Possible mechanisms that contribute to jet breakup and atom-

9

ization in this regime include the nozzle geometry, cavitation and turbulence within the nozzle, aerodynamic instabilities and relaxation of the boundary layer as the fluid flows out of the nozzle. For the flow parameters considered here, the jet, as it leaves the nozzle, is slightly supersonic relative to the ambient air. We model the flows as compressible.

Nozzle flow plays an important role in primary jet breakup. Cavitation, commonly formed in high pressure injectors, is found to have strong effect on the flow at the exit of the nozzle [1]. Two phases (liquid and vapor) are involved in the nozzle cavitation, as well as two equations of state (EOS), or two branches of a common EOS. The free surface between vapor and liquid as well as that between the liquid and the ambient gas (with its own EOS) are modeled in *FronTier*. We use the cavitation model proposed in [64]. This model involves two numerical parameters, the cavitation bubble size and spacing at the time of bubble formation, and one physical parameter, the critical pressure for vapor bubble formation.

2.2 Numerical models

The fuel and gas are both modeled as compressible fluids. A TVD scheme [29] is used to obtain the states at cell centers. A ghost fluid method is used to couple the interface with the fluid solver. The surface tension force is modeled as a pressure jump across the interface. Second order normal vectors and first order curvature tensors are calculated from a local polynomial approximation on the interface [25]. Cavitation bubbles are modeled by a discrete bubble insertion model [64]. Subgrid scales are modeled by a Smagorinsky type subgrid model [31, 41]. An analysis of the droplet diameter distribution is performed at the final time of the 3D simulation.

2.2.1 Cavitation model

Classical nucleation theory (CNT) has been developed by many authors, see [3, 52] and references therein. Xu *et.al.* performed 2D nozzle flow simulations with CNT cavitation model [64]. However, there is a large discrepancy between computation results from this theory and experimental measurements of nucleation thresholds, caused by impurity induced nucleation sites. N-heptane cavitates at -300 bar at 300 K predicted by CNT, while experimental measurement gives -50 bar [60]. Accordingly, we use -50 bar in our simulations. The sensitivity to this parameter is examined in Sec. 3.3.

2.2.2 Subgrid models for turbulence

The compressible Navier-Stokes equations are solved in the fluid and gas regions separately. In order to resolve all the flow scales, it would be necessary to have the mesh size smaller than the Kolmogorov scale. In our simulations for the nozzle flow, the estimated Kolmogorov scale is less than 10^{-1} μm near the nozzle exit. Since such a mesh is impractical, a coarse mesh with a dynamic LES approach is used to represent all the flow scales. A Smagorinsky type sub-grid model is used, with all coefficients computed dynamically, through comparison of modeled and averaged terms on two adjacent grid levels [31, 41].

2.2.3 Droplet diameter and distribution

We measure droplet diameters and their probability distribution in our simulations. We study two characteristic diameters for diesel spray, mass median diameter (MMD) and Sauter mean diameter (SMD). The MMD is the droplet diameter that

divides the total mass of droplets in half. SMD is defined as

$$\text{SMD} = \frac{\sum D_i^3}{\sum D_i^2} \,, \tag{2.1}$$

where D_i is the droplet diameter. The droplet diameter distribution is also compared with a log-normal distribution model, which is commonly used to model the droplet diameter distribution after primary breakup [65].

$$f(D) = \frac{1}{\sqrt{2\pi}\sigma_{\ln}D} \exp\left[-\frac{[\ln(D/D_{\ln})]^2}{2\sigma_{\ln}^2}\right] \,. \tag{2.2}$$

This model has two free parameters. $\sigma_{\ln}$ is the non-dimensional standard deviation of the logarithm of the diameter and $D_{\ln} = \exp\left[\overline{\ln D}\right]$ is the log-normal diameter defined as the exponent of the logarithm average.

2.2.4 Other models

We use a stiffened gamma law [40] to model the equation of state of liquid jet,

$$p + \gamma p_\infty = (\gamma - 1)\rho(e + e_\infty) \,, \tag{2.3}$$

where the adiabatic coefficient $\gamma = 3.19$, the stiffening constant $p_\infty = 3000.5bar$ and $e_\infty = 4851.6cm^2/ms^2$. The polytropic gamma law [40] gas is used for the ambient gas and vapor gas. We can calculate the change of pressure with the change of internal energy by using

$$\Delta p = (\gamma - 1)\rho\Delta e \,. \tag{2.4}$$

We also use the Discrete Vapor Bubble Model and Phase Transition model introduced in [63].

Chapter 3

Diesel spray simulations

3.1 Introduction

The mechanism of the atomization process of a high speed jet has been studied extensively in theory [32, 47, 48] and experiments [33, 38]. Primary jet breakup remains a challenging research topic due to the large range of scales (spatial and temporal), and the complex flow regimes involved. Experimental observations are difficult because the droplets in the spray from the breakup obscure the spray interior and the liquid core.

Numerical simulation appears to be a promising method to study the details of the breakup process of the liquid jet. However, the physical process of atomization poses difficulties for numerical algorithms. First, as the fuel has a much higher density than the ambient air, an accurate algorithm to deal with the interface between these two is required. Secondly, since the growth of perturbations on the interface is one of the important mechanisms in atomization [47], the algorithm should have small numerical diffusion so as not to suppress this process. Since one of the characteristics of atomization is topological change, such as breakup and merging of the interface, the algorithm must also resolve topological change robustly. During atomization, droplets

whose diameter is much less than that of the nozzle are generated, and consequently, a high resolution algorithm is required to resolve small droplets. Third, liquid cavitation occurs inside the nozzle, mitigating pressure disturbances and influencing turbulence in the flow, as well as atomization [63].

From linear stability theory, the flow leading to liquid jet breakup is divided roughly into four parameter regions, according to the flow Reynolds number and Weber number [27]. Here we are concerned with high speed jets, well within the third of these regimes, called the second wind driven regime. Generally, jet breakup and atomization in this regime is caused by the growth of waves which originate at the nozzle exit. These waves eventually break up the jet core when the amplitude reaches a certain value [32]. The initial disturbance of the jet is provided by the turbulent and cavitation flow in the nozzle. The flow conditions inside the nozzle has large contribution to jet breakup [22]. These flow conditions include the nozzle geometry, cavitation and turbulence within the nozzle, and relaxation of the boundary layer as the fluid flows out of the nozzle.

In this chapter, we first study the flow inside the nozzle. The development of the turbulence and the cavitation inside the nozzle is investigated numerically. We then study the primary breakup of the high speed liquid jet numerically. The breakup of the jet tip is observed in our simulations.

3.2   Nozzle flow

In this section, we present the results of numerical simulations of the flow in the nozzle. In the simulations, fluid and jet nozzle parameters have been chosen that are typical of diesel injection, following experiments performed at ANL [44]. The nozzle diameter is 0.178 mm and its length is 1 mm. A finite pulse of diesel fuel is injected

into a chamber of SF_6 (a heavy, inert gas chosen to emulate the density of compressed air in a diesel engine). In 0.3 μs, the pressure of injected fuel rises linearly from 1 bar to 500 bar, then it is maintained at this level for 0.4 μs, and subsequently, it drops linearly to 1 bar over 0.1 μs. 2D simulations are performed with a 2D axis-symmetric nozzle geometry. Due to the relatively low computational cost, both the nozzle and the combustion chamber are considered for 2D simulations. 3D simulations are performed only in a quarter nozzle to reduce the computational burden. The 3D jet simulation in the combustion chamber will be considered in Sec 3.5. The liquid density is $0.66g/cm^3$; its viscosity is 0.013 Poise. The Reynolds number is 31,600 at quasi-steady state. For 2D and 3D simulations, the surface tension between liquid and gas is $0.02N/m$. The Weber number at quasi-steady state is 720,000. The grid size is $2.2\mu m$ in both 2D and 3D simulations. Our two main results are a strong dependence of the turbulence level on cavitation and the overall similarity of the 2D and 3D mean velocity. Some differences in detail between 2D and 3D are also noticed.
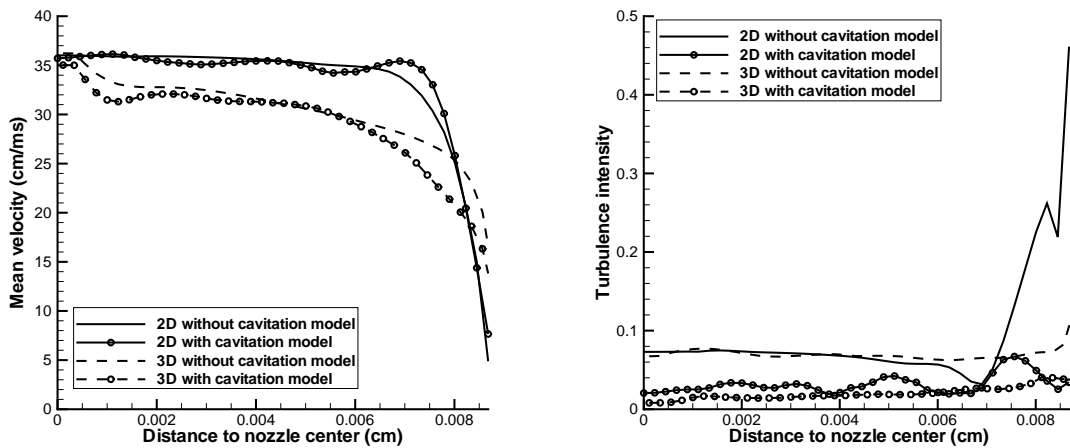

Figure 3.1: Stream-wise velocity profiles (Left) and stream-wise turbulence intensity (Right) along a radial direction just upsteam the exit of the nozzle.

15

We compare the averaged stream-wise velocity profiles and turbulence intensity along a radial direction just upsteam of the exit of the nozzle when both 2D and 3D flows achieve quasi-steady states, see Fig 3.1. Here the averaged stream-wise velocity has been averaged over 100 time steps to remove fluctuations. The turbulence intensity in each point is defined as:

$$I = \frac{u'}{\bar{u}}, \ u' = \sqrt{\langle \delta u, \delta u \rangle}, \tag{3.1}$$

δu is the point-wise velocity fluctuation, which can be defined as

$$\bar{u}(r,z) = \frac{1}{T_2 - T_1} \int_{T_1}^{T_2} u(r,z,t)dt,$$

and $\bar{u}$ is the mean stream-wise velocity, which can be defined as

$$u'(r,z) = \Big[\frac{1}{T_2 - T_1} \int_{T_1}^{T_2} [u(r,z,t) - \bar{u}(r,z)]^2 dt\Big]^{1/2}.$$

The brackets represent averaging over time. These u' is the root-mean-square of the stream-wise turbulent velocity fluctuation. Although cavitation model has no strong effect on the mean stream-wise velocity, it influences the stream-wise turbulence intensity. Without the cavitation model, the strong rarefaction waves generated in the sharp nozzle inlet are reflected between the nozzle wall and enhance the velocity fluctuation. With the cavitation model, the strong rarefaction waves are relaxed due to the high compressibility of the cavitation bubbles. The Reynolds number $Re = 31,600$ exceeds the critical value for transition to turbulence. However, due to the short length of the nozzle, the turbulence does not reach its predicted asymptotic steady state value, which for this flow would be around 0.056 [24]. Heukelbach et.al. [21] measured the stream-wise turbulence intensity for a cavitating nozzle with

16

$Re = 8500$ and nozzle length-diameter ratio 4. They found the stream-wise turbulence intensity is between 0.01 and 0.02 near the nozzle center and is 0.03 near the nozzle wall. The stream-wise turbulence intensity from our simulations is in this range, and is reasonable considering the larger nozzle length-diameter ratio and the larger Reynolds number. The integral length scale measured in our simulation near the nozzle exit is $0.38R$ which is large than $0.25R$ for fully developed pipe flow [24] due to the short nozzle length in our simulation.

Turbulence is intrinsically a 3D phenomenon, Turbulence theory [24] predicts significant differences between 2D and 3D flow. For a 2D flow, there is no stretching effect and vorticity is convected but is not changed by the flow. This can be clearly noticed in the vorticity plot in Fig. 3.2. The 2D vorticity generated in the nozzle inlet is moving along the nozzle wall downstream. For a 3D flow, the stretching effect changes both the magnitude and the direction of vorticity vectors. Fig. 3.2 shows that the 3D vorticity in the nozzle inlet spreads downstream. This may also affect the mean stream-wise velocity profile, as can be seen in Fig. 3.1.
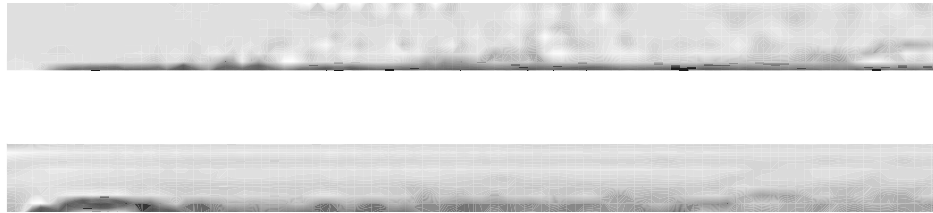

Figure 3.2: Vorticity contour in 2D (upper) and 3D (lower) nozzle flow simulations in a quasi-steady state. The 3D contour is from the average over the azimuthal direction. The flow is from left to right.

3.3 2D breakup and cavitation model parameters

A discrete vapor bubble model, to model cavitating, or multiphase flow, was proposed in [64], but neither the numerical parameters (cavitation bubble size and spacing) nor the physical parameter (critical pressure) were studied thoroughly. We study this model systematically in this section.

Since the experimental data of [44] concerns the breakup of the jet, and since breakup is only weakly sensitive to the cavitation model parameters, we determine only an approximate range for these parameters. We select apparently optimal values for the three model parameters (to define what we call the base case). We compare results with variation of these parameters and with no cavitation model present. Here the "base case" stands for a cavitation bubble diameter 6 mesh blocks, inter-bubble spacing 1 bubble diameter, and critical pressure for bubble insertion -50 bar. We vary the three parameters in our simulations and compare the results with those from experiments. The experimental comparison includes the jet tip velocity and the mass flux through an observational window. The observational window is located on the spray axis 1 mm from the nozzle, with a size 500 $\mu m \times 50$ μm. The measurements of the mass flux through this window reflect the degree of jet breakup; as the mass within the window decreases, there is more breakup.

Fig. 3.3 shows the jet surface for the base case. Without the cavitation model, strong rarefaction waves exist inside the nozzle. The unphysical pressure minimal can reach as low as -400 bar. With the cavitation model, no such strong pressure waves are formed, as the compressibility of the bubbles mitigates the transient pulses which would otherwise yield strong pressure fluctuations. Once the pressure falls below a critical value, a vapor bubble is inserted, and thereby the unphysical pressure wave is suppressed. The breakup of the base case is due to turbulent fluctuations within

18

the jet, yielding surface instabilities that grow dynamically, reinforced by interactions between the ambient gas and the liquid core surface. The comparison between the simulation result with and without the cavitation model is presented in the appendix.
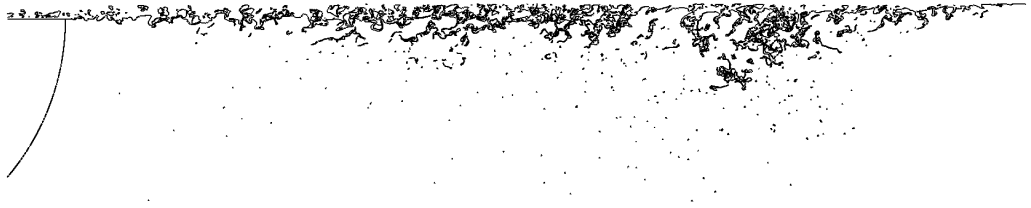
Figure 3.3: Late time jet surface from a 2D simulation.

The mass observed within the observational window and tip jet velocity plot are show in Fig. 3.4. The cavitation model has better agreement with experiment results. Fig. 3.5 shows the influence of the cavitation bubble diameter (4, 6, 8 mesh blocks) on the tip velocity and mass flux. The bubble spacing, one bubble diameter, and the critical pressure, -50 bar, are fixed for these simulations. For all three cases, the simulation results show the same trend as the experimental results. However, the agreement is not perfect in any of the cases, and the dependence of the results on cavitation bubble diameters is weak, so that we could say that the parameter is insensitive, and is not tightly constrained by the experimental results. Fig. 3.6 shows influence of bubble spacing. The inserted cavitation bubble diameter and critical pressure are fixed. Both the tip velocity and the mass flux are insensitive to this parameter. Fig. 3.7 shows the influence of critical pressures with values -5, -50, -200 bar. For critical pressure -5 bar case, excessive bubbles are inserted into the liquid

19
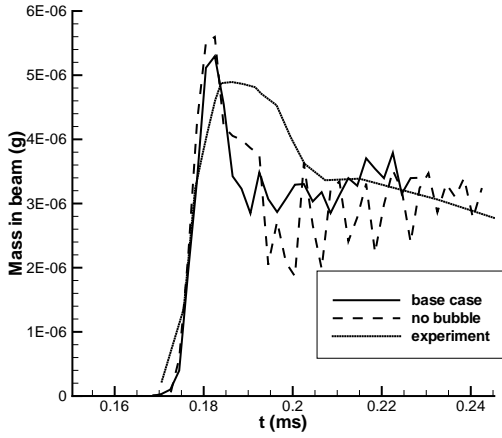
(a) Mass through a window vs. time
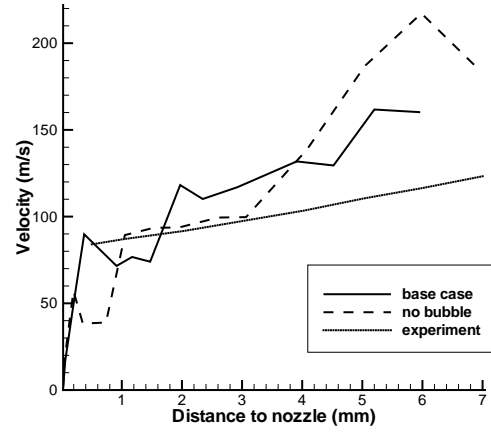
(b) Velocity vs. tip penetration

Figure 3.4: A comparison of the tip velocity and mass flux among the base case, without cavitation model case and experimental results.
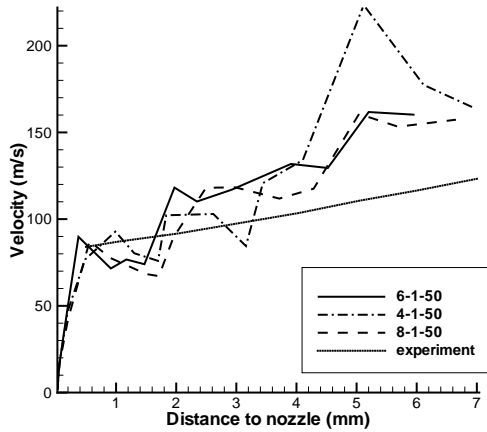
(a) Velocity vs. tip penetration
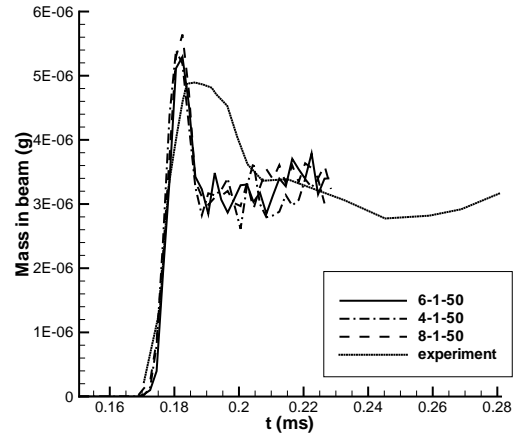
(b) Mass through a window vs. time

Figure 3.5: Influence of cavitation bubble diameters. The line labels x-y-z in the legend refer to the three cavitation model parameters respectively: initial cavitation bubble diameter, spacing, and critical pressure.

and the tip velocity is much higher than the experimental value. For the critical pressure -50 and -100 bar cases, the results show reasonable agreement with those from experiment.

We show evidence to suggest that the cavitation model is important in the simulation of jet breakup. The parameters of our model do not seem to be very sensitive, but preferred model parameters are a cavitation bubble diameter 6 mesh cells, bubble spacing 1 bubble diameter and critical pressure -50 bar.

(a) Velocity vs. tip penetration

(b) Mass through a window vs. time
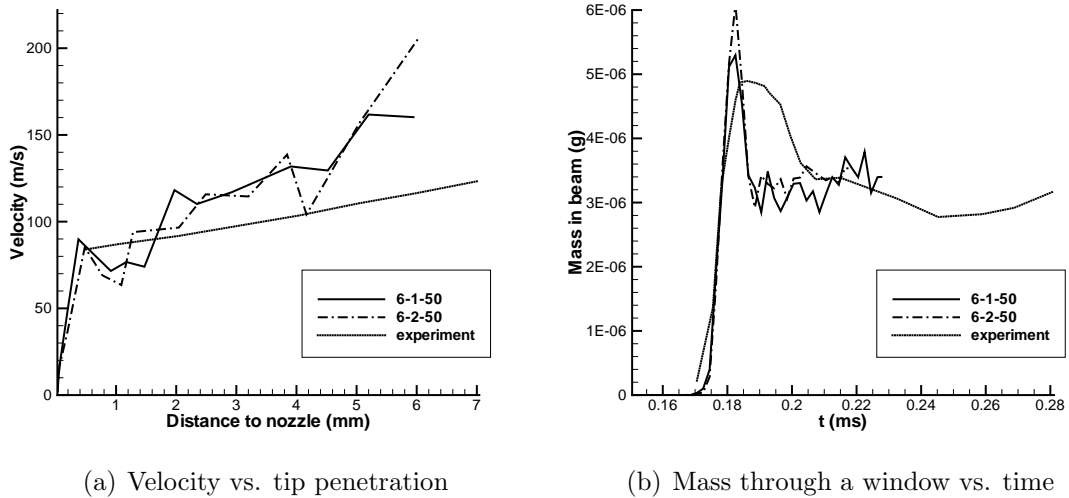
Figure 3.6: Influence of cavitation bubble spacing

3.4   2D simulations of breakup

The computational efficiency of the 2D simulations allow more study on pdf of the droplet size distribution. The pdf is visually well fit by a log normal distribution, as is expected from experimental studies. We find an excess of large droplets in comparison to this fit. These large droplets skew the determination of the Sauter mean diameter (SMD). Large droplets are ligaments just detached from liquid core.

21

(a) Velocity vs. tip penetration

(b) Mass through a window vs. time
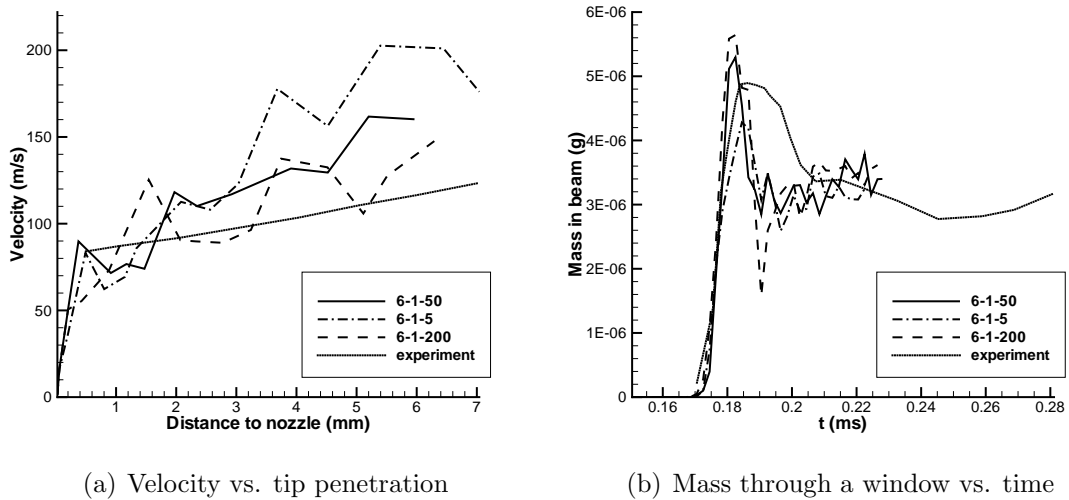
Figure 3.7: Influence of critical pressure

they are unstable to further breakup, and we do not comment on possible causes for this effect (time of observation, 2D vs. 3D, grid resolution effects). In Fig. 3.8, the pdfs for two levels of grid refinement are compared, each with a best fit log normal distribution superimposed. The log-normal distribution agrees well with simulations.

To clarify the mechanism of primary jet breakup, we study the growth of the surface waves in the 2D simulation with 1 micrometer grid. As the simulation reaches a steady state, we draw the surface plots near the nozzle outlet every 100 steps in one graph, and the envelope of the jet surface is plotted in Fig 3.9. From linear stability analysis [32], the envelope represents the edge of the fastest growing wave. The wave length for the fastest growing wave is 38 micrometers which can be measured from the surface plot. From the linear stability theory, the expression for the growth rate

22
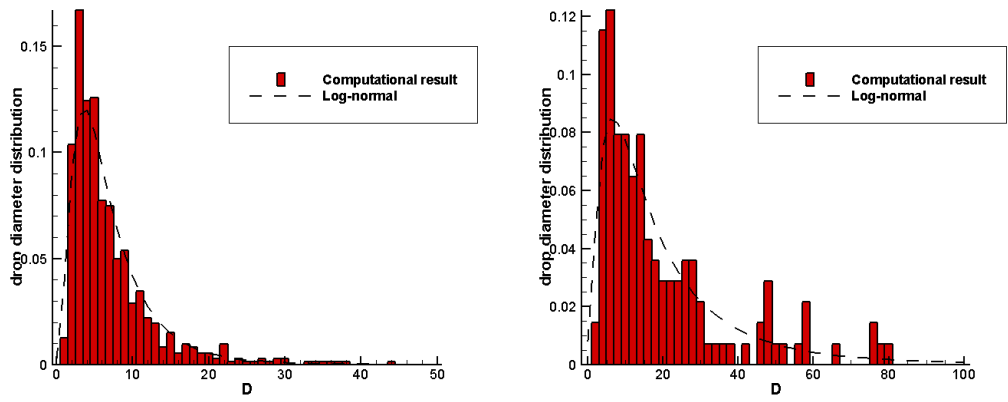
Figure 3.8: Droplet diameter distribution for grid size $1\mu m$ (left) and grid size $2\mu m$ (right)
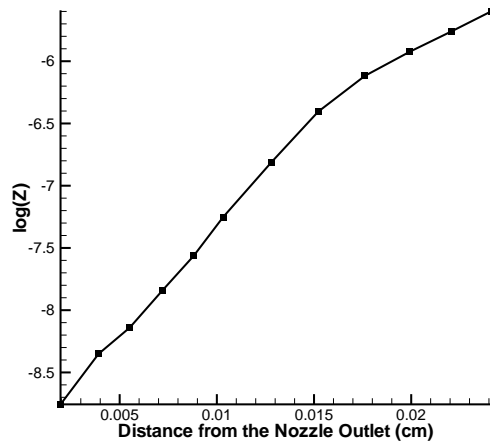
Figure 3.9: The envelope of the time averaged jet surface.

ω in the regime we consider was presented by Levich [28] as the following equation

$$\omega^2 = (\rho_G k^2 U^2 - \sigma k^3)/\rho_L \ , \qquad (3.2)$$

where ρ_G and ρ_L are the air and the liquid density. k is the wave number. Equation 3.2 gives the theoretical growth rate for the fastest growing wave. From Fig 3.9, the growth rate of the fastest growing wave from our simulation agrees with that estimated from equation 3.2. We conclude that the growth of surface waves are mainly driven by aerodynamic interaction in the early stage of jet breakup.

3.5   3D simulations of breakup

Many mechanisms are found to be responsible for primary breakup. Aerodynamic theory [46, 55] was first proposed. This theory postulated that primary breakup is due to aerodynamic interactions between the liquid and the gas leading to unstable wave growth on the liquid jet surface. Reitz *et al.* [47, 48] reported several experimental investigations where the spray angle was measured. The effect of ambient pressure, density ratio, and viscosity ratio was studied. They found that results were consistent with the aerodynamic theory. Wu *et al.* [62] and Sallam *et al.* [51] proposed that primary breakup is initialized by the turbulence of the liquid jet. They assume the onset ligament diameter is equal to the onset eddy size and that droplets are formed due to Rayleigh breakup of the corresponding ligaments. Their correlations show agreement with their experimental droplets sizes. Arcoumanis *et al.* [1] found that cavitation induced in the nozzle enhances the turbulence level near the nozzle exit and thus helps the breakup of the liquid core. Dumouchel [12] summarized many experiments. He concluded that the nozzle flow has a strong influence on the primary breakup in the second wind-induced and atomization regimes. He also concluded that

24

aerodynamic forces are unimportant in primary breakup for density ratios larger than 500.

Our simulations support the following mechanism of breakup. Nozzle turbulence drives the initial jet instability. Once initialized, these modes grow into liquid films due to a Kelvin-Helmholtz instability. The films are themselves unstable, and become ligaments, Finally the ligaments break up into droplets, in a Rayleigh instability mode.

Many 3D numerical simulations have been performed to study the details of primary breakup. Due to the large range of temporal and spatial scales, these simulations still remain very challenging. Using VOF-LES simulations, Bianchi *et al.* [4] performed simulations under both laminar and turbulent conditions. The results confirm the role of turbulence in determining the onset of jet surface breakup. Using a refined level set grid method, Herrmann [20] simulated primary breakup with several levels of grid. The resulting droplet size distributions are of log normal type for different grid sizes. The mesh independence of the large droplets is achieved. However, the resulting SMD is not compared with experimental results. Desjardins *et al.* [10] reported results for turbulent jet atomization using a conservative level-set method coupled with a ghost-fluid method. Menard *et al.* [39] employed the CLSVOF method to study the breakup of a turbulent jet. However, the distribution of the droplet sizes was not studied in their papers.

In recent results, we perform a 3D simulation in the computational domain $3R \times 3R \times 40R$, where $R = 0.089cm$ is the nozzle radius. Only a quarter of the jet is simulated considering the rotational symmetry of the jet. The parameters in our simulation are summarized in Table 3.1. The Weber number and density ratio have been decreased by factors of 5 and 4 respectively from Parker *et.al.*'s experiments [42] to make the simulation feasible. The jet is in the second wind induced regime with these parameters. The whole region is discretized by using a uniform cartesian mesh

25

Table 3.1: Parameters for 3D jet breakup simulation.

liquid density	0.66 g/cm^3	density ratio	10
ambient density	0.066 g/cm^3	Reynolds number	20,380
nozzle diameter	0.089 cm	Weber number	$2,200$
jet velocity	200 m/s	Ohnesorge number	0.0023
surface tension	2.4 N/m^2		
fluid viscosity	0.013 Poise		
ambient pressure	40 bar		
mesh size	2.2 μm		

$120 \times 120 \times 1600$. At the beginning of the simulation, the domain is filled with high pressure gas. The liquid jet is injected from the left side of the domain. The inlet turbulent velocity is given by a filter based generator with a prescribed length scale [26]. In our simulation, the integral length scale $\Lambda = 0.38R$ is from the nozzle flow simulation in Sec. 3.2. The turbulence intensity is 0.056 of the mean inflow velocity. Reflecting boundary conditions are used on the planes $y = 0$ and $z = 0$. All other boundaries are modeled as flow through.

Fig. 3.10 shows the snapshots of the jet surface [6][8]. In the figure, a quarter jet is reflected to form a whole jet for better visualization. The jet has a clear intact core near the nozzle exit, as is noticed in X-ray images [44]. The surface instability is first initialized by the inflow turbulence. Then, these instabilities grow into films due to the Kelvin-Helmholtz instability. Finally, the films are unstable and break up into filaments, which further break up into droplets. Liquid films, filaments and droplets can be observed from Fig. 3.11 which shows a detail of the jet surface in the end of the simulation [6][8].

We evaluate the distribution of droplet diameters in the simulation. In Fig. 3.12, probability density function (PDF) of droplet diameters and its log normal fit are plotted together [6][8]. The PDF follows a log normal distribution as expected by

26

many experiments [27]. We compare the resulting SMD with Wu $et.al.$'s correlation [61],

$$\text{SMD}/\Lambda[1 + 0.04(\rho_g/\rho)(\bar{u}_0/\bar{v}_0')^2(\Lambda/\text{SMD})^{2/3}]^{3/5} = 76(We_{f\Lambda})^{-0.69}. \qquad (3.3)$$

Here $\bar{u}_0$ and $\bar{v}_0'$ are the averaged stream-wise velocity and root mean square velocity in the nozzle exit, Λ is the integral turbulence length scale, $We_{f\Lambda}$ is the liquid Weber number with Λ as the length scale. The SMD from (3.3) is 25 μm which is close to 20 μm from the simulation. Fig. 3.12 shows the SMD from the simulation and those from Wu $et.al.$'s experiments along with the correlation. We also study the range of the droplet diameter distribution. The ratio of the mass median diameter (MMD) to the SMD is proposed to describe the width of the droplet distribution [27]. Many authors found the relation MMD/SMD $= 1.2$ to hold after primary breakup for direct injection nozzles [54, 61]. We obtain MMD/SMD$=1.23$ from the simulation, which means that the droplet diameter distribution is nearly equal but slightly wider than that in experiments.
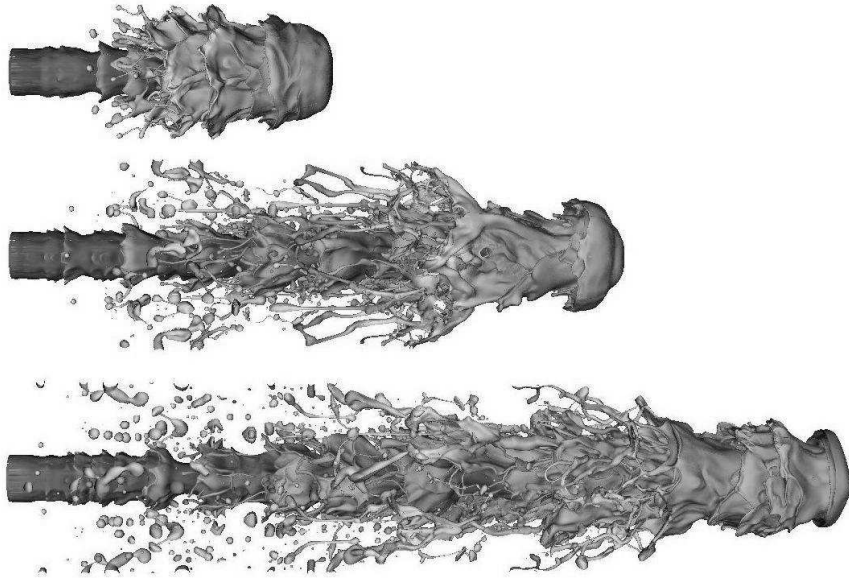
Figure 3.10: Snapshots of the 3D jet surface.
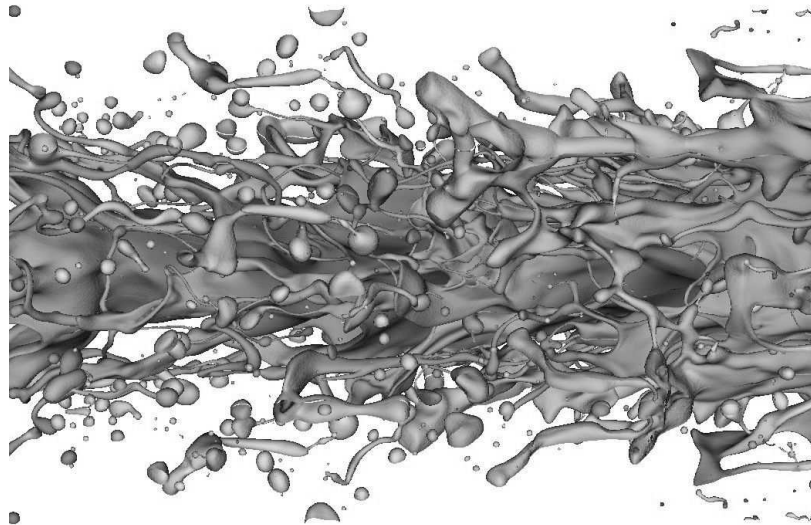
Figure 3.11: The detail of the jet surface at the end of the simulation.
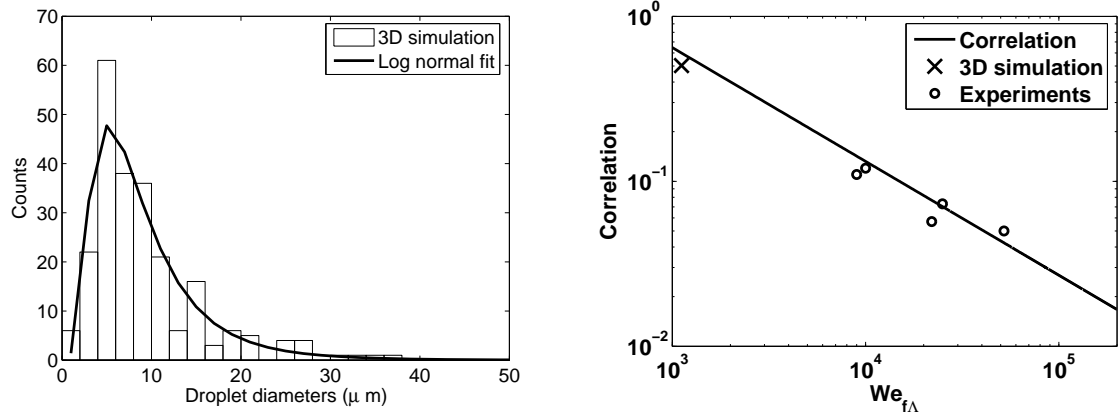
Figure 3.12: Left: Droplet diameter distribution from the 3D simulation. Right: The SMD from the simulation and the correlation from [61], and the correlation formula is the left side of equation 3.3.

Chapter 4

Rayleigh instability and Kelvin-Helmholtz instability

As we mentioned earlier, aerodynamic instabilities play an important role for jet breakup and atomization. We conduct a series of simulations to demonstrate that *FronTier* can handle those mechanisms properly.

4.1 Kelvin-Helmholtz instability

4.1.1 Introduction

The Kelvin-Helmholtz instability arises when two fluids are separated by an interface across which the tangential velocity is discontinuous. Such a flow is unstable under a sinusoidal perturbation of the interface. The Kelvin-Helmholtz instability plays an important role in the primary breakup of a liquid jet especially for high pressure combustors [47, 49]. The evolution of the 2D Kelvin-Helmholtz instability has been studied by theory [2, 43] and by numerical simulations [19, 23, 56].

Here we investigate numerically the Kelvin-Helmholtz instability with surface tension using the compressible Euler equations. We first consider the Kelvin-Helmholtz instability in the linear (small amplitude) regime. In a 2D domain $[-1, 1] \times [-2, 2]$,

two fluids are initially separated by a perturbed interface. The fluid below the interface is moving with velocity U_1 and the fluid above is moving with velocity U_2. The density of the bottom and top fluids are ρ_1 and ρ_2, respectively. The computational domain has periodic horizontal boundaries and rigid, no slip walls at the top and the bottom. The domain length is the wavelength λ. The interface is perturbed by a sinusoidal wave with amplitude

$$A = Im[A_0 e^{ik(nt+x)}] \tag{4.1}$$

where $k = 2\pi/\lambda$ is the wave number, n is the growth rate and A_0 is the initial amplitude of the perturbation. For a small initial amplitude, the growth rate can be predicted by the linear stability theory. For compressible fluids, we have the dispersion relations [43]

$$\rho_1(n+U_1)^2 \left/ \sqrt{1 - \frac{(n+U_1)^2}{c_1^2}} + \rho_2(n+U_2)^2 \right/ \sqrt{1 - \frac{(n+U_2)^2}{c_2^2}} = \sigma k^2, \tag{4.2}$$

where σ is the surface tension coefficient and c_i is the sound speed for fluid i. As c_1 and c_2 approach infinity, the denominators on the left side the the equality go to unity and (4.2) converges to the dispersion relation for incompressible fluids [9],

$$\rho_1(n+U_1)^2 + \rho_2(n+U_2)^2 = \sigma k^2. \tag{4.3}$$

Here we introduce a dimensionless time

$$\tilde{t} = tk\Delta U, \quad \Delta U = |U_2 - U_1|. \tag{4.4}$$

All times used below are given in these dimensionless units. The Weber number is

31
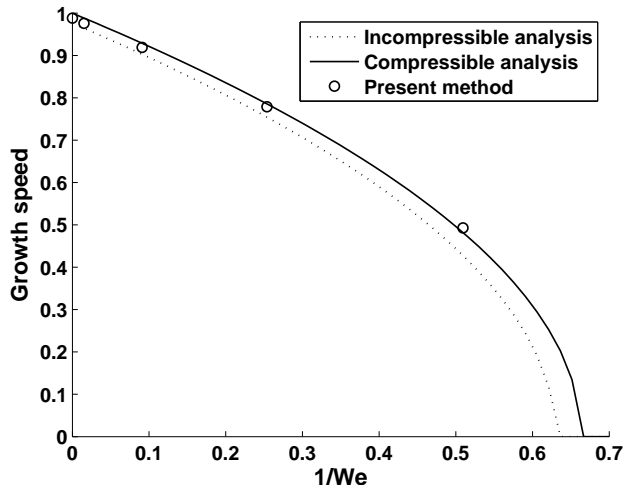
Figure 4.1: Initial dimensionless growth rate vs. inverse Weber number for a $M = 0.2$ Kelvin-Helmholtz instability with density ratio $\rho_1/\rho_2 = 20$. Simulations are performed under a 80×160 mesh.

defined as

$$We = \frac{\rho_2 \Delta U^2 \lambda}{\sigma}. \tag{4.5}$$

Following Tauber *et al.* [56],

4.1.2   Simulation results

We investigate Kelvin-Helmholtz instability with density ratio $\rho_1/\rho_2 = 1$ and $\rho_1/\rho_2 = 100$. In our simulations, the initial amplitude is taken to be 2.5% of the wavelength. We first study the convergence of the growth rate using 40×80, 80×160, 160×320 and 320×640 meshes. We then study the late time behavior of the Kelvin-Helmholtz instability up to a time $\tilde{t} = 60$

In Figure 4.1, the computed initial growth rate is plotted vs. the inverse Weber number for density ratio 20 [7][8]. The growth rate is normalized by the maximum growth rate. Here the Mach number is $M = 0.2$. The solid line is the growth rate

32

Table 4.1: The relative errors for the growth rate of the Kelvin-Helmholtz instability.

Mesh	40×80	80×160	160×320	320×640
Present method	0.083771	0.031346	0.020572	0.009487
FT	0.037861	0.023490	0.011997	0.009287
FT/GFM	0.072810	0.030254	0.021237	0.009331

predicted by (4.2). The dashed is the growth rate predicted by (4.3). Open circles represent results from FT/GFM. A 80×160 mesh is used in the simulation. The growth rate agrees with the linear stability analysis for compressible fluids. Due to the small Mach number, the growth rates predicted by the compressible and incompressible analysis show little difference.

In Table 4.1, the relative errors of the growth rate under different resolutions are given for density ratio $\rho_1/\rho_2 = 1$ [7][8]. To eliminate the sensitivity of the growth rate to the time used for data collection. we compare the following averaged growth rate for the three methods at early time,

$$\tilde{n} = \int_0^{\tilde{t}_0} n(t)dt, \ \tilde{t}_0 = 6. \tag{4.6}$$

First order convergence is observed for all three front tracking methods. The relative error of the present method is comparable to the method in [57], but is larger than our previous front tracking method.

We also study the long-time evolution of the Kelvin-Helmholtz instability for Weber number, $We = 6$. This case is also studied by Tauber *et al.* [56]. Figure 4.2 shows the temporal evolution of the interface for $We = 6$ with the present tracking methods [7][8]. For early times, the growth rate is consistent with that predicted by the linear stability theory. As two fingers continue to grow and extend to the opposite fluid, viscous effects increase the thickness of the shear layer and the fingers

33
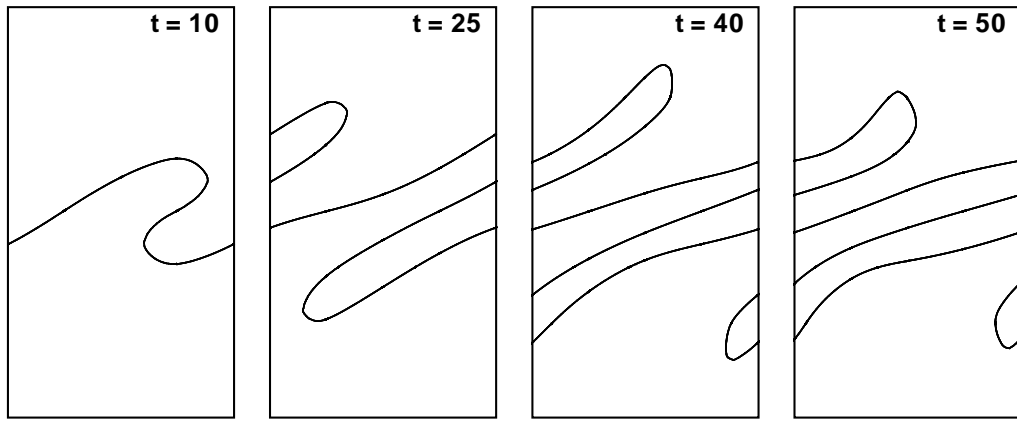
Figure 4.2: Interface at $t = 10, 25, 40$ and 50 for $We = 6$ and $Re = 5000$.

are pulled back by surface tension force. A similar behavior has been observed in the simulations of Tauber *et al.* [56] and Herrmann [19].

4.2 Rayleigh instability

4.2.1 Introduction

Rayleigh instability, explains why and how a falling stream of fluid breaks up into smaller packets with the same volume but a smaller surface area. The driving force of the Rayleigh instability is that liquids, by virtue of surface tension, tend to minimize their surface area. According to Young-Laplace equation,

$$\Delta p = \gamma(\frac{1}{R_1} + \frac{1}{R_2}) \tag{4.7}$$

the pressure due to surface tension is increased as the radius of the stream is smaller and decreased as the radius is greater. If there is small perturbation of the cylindrical stream surface, the stream becomes unstable. Here Δp is the pressure difference across the fluid interface, γ is the surface tension, R_1 and R_2 are the principal radii of curvature(radius and radius of curvature). The radius of curvature can be negative,

Table 4.2: The relative errors of the growth rate for Rayleigh instability.

Mesh	15×50	30×100	60×200
Present method	0.11100	0.062362	0.032646
FT	0.13096	0.065040	0.033261
FT/GFM	0.12992	0.086966	0.048113

meaning that, according to Young-Laplace, it actually decreases the pressure across the surface of the stream. Likewise the radius of curvature is positive and increases the pressure in that region. The detailed description for the calculation of the curvature and the source term for Navier-Stokes equation is presented in the appendix.

4.2.2 Simulation results

Four different regimes describe the phenomenology of liquid jet breakup. The first of these with the smallest values of ΔU was studied theoretically by Rayleigh [45] using linear stability theory. For $\Delta U = 0$, a stationary jet whose length is longer than its perimeter is unstable under surface tension forces. Any disturbance can initiate the growth of a wave along the jet that will lead to break-up.

We perform simulations in a 3D domain $[-3r, 3r] \times [-3r, 3r] \times [0, \lambda]$ and in a 2D domain $[0, 3r] \times [0, \lambda]$, where $r = 2 \times 10^{-4}$ cm is the radius of the jet, λ is the wave length. The computational domain has periodic conditions in x, y and z directions. Following the linear stability theory, a sinusoidal perturbation is imposed in the initial time:

$$A = Im[A_0 e^{ikz}] \tag{4.8}$$

where A_0 is the initial perturbation amplitude, set to $2.5\%\lambda$. We keep the grid spacing to 20 cells across the radial direction of the liquid column and change the disturbance wavelength λ. We compute the non-dimensional growth rate β/β_0, where

35
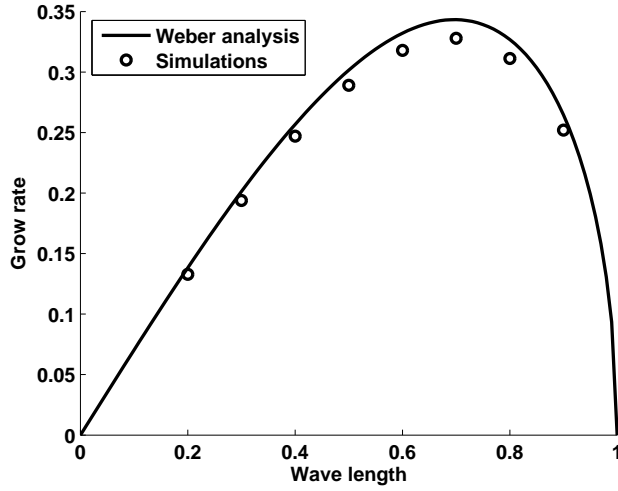
Figure 4.3: Dispersion relation for Rayleigh instability.

$\beta_0 = \sqrt{\sigma/(\rho_g r^3)}$. The growth rate is a function of the non-dimensional wave number $\eta = 2\pi r/\lambda$. We compare our results to the linear stability theory of Weber [59] in Figure 4.3 [7][8].

We then compare the results for $\lambda = 10r$ using 15×50, 30×100 and 60×200 meshes. The relative errors for the growth rate are summarized in Table 4.2 [7][8]. Both methods have a first order convergence rate in early time. The present method is more accurate than our previous method.

We compare the results obtained by 2D and 3D front tracking methods. Figure 4.4 shows the temporal evolution of the interface using the present method and the previous method under a 30×100 mesh [7][8]. Both methods give similar results.
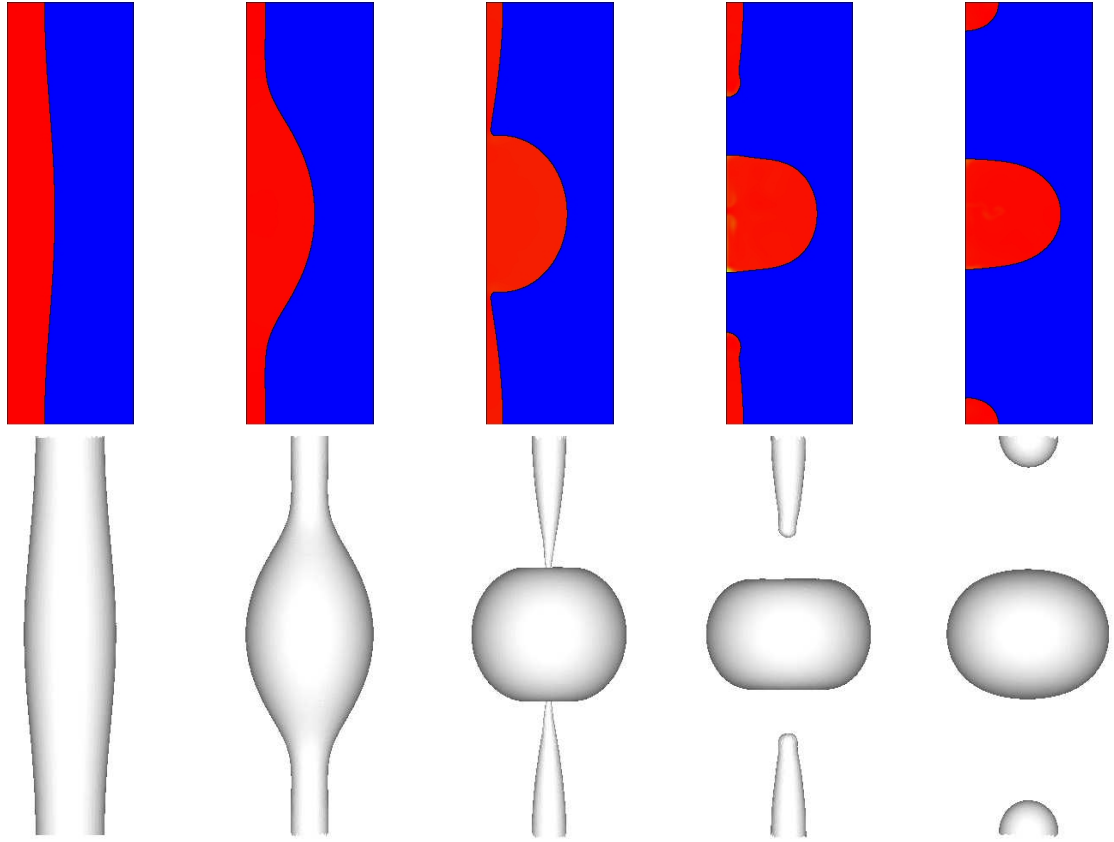
Figure 4.4: Evolution of the interface for Rayleigh instability. Top: 2d method, Bottom: 3d method.

Chapter 5

Conclusions

A front tracking method is used to study the primary breakup of high speed liquid jets. We perform both 2D axisymmetric and 3D simulations for the nozzle flow and liquid jet breakup.

In the nozzle flow simulations, the geometry of the nozzle is from ANL's experiment [44]. We find 2D-3D agreement for the mean velocity in the nozzle exit and the occurrence of cavitation. We also find the differences in the vorticity structure and turbulence level.

We explore the physical and numerical parameters in the cavitation model of 2D simulations. We find the breakup is only weakly sensitive to these model parameters. For these simulations, we find agreement with experiment in regard to the tip velocity of the jet and its overall degree of breakup or spreading. A 3D simulation is performed under liquid Weber number 2,200 and liquid-gas density ratio 10. The detailed process of the jet breakup is identified in the simulation. The droplet diameters follow a lognormal distribution. The SMD is 20 μm and MMD/SMD = 1.23, both in agreement with experimental correlations.

Bibliography

[1] C. Arcoumanis, H. Flora, M. Gavaises, N. Kampanis, and R. Horrocks. Invectigation of cavitation in a vertical multi-hole injector. *SAE Technical Papers 1999-01-0524*, 1999.

[2] Gregory Baker and André Nachbin. Stable methods for vortex sheet motion in the presence of surface tension. *SIAM J. Sci. Comput.*, 19(5):1737–1766, 1998.

[3] S. Balibar and F. Caupin. Metastable liquids. *J. of Physics: Condensed Matter*, 15:s75–s82, 2003.

[4] G. M. Bianchi, F. Minelli, R. Scardovelli, and S. Zaleski. 3d large scale simulation of the high-speed liquid jet atomization. *SAE Technical Papers 2007-01-0244*, 2007.

[5] W. Bo, B. Fix, J. Glimm, X. L. Li, X. T. Liu, R. Samulyak, and L. L. Wu. Frontier and applications to scientific and engineering problems. *Proceedings of International Congress of Industrial and Applied Mathematics*, pages 1024507–1024508, 2008.

[6] W. Bo, X. Liu, J. Glimm, and X. Li. Primary breakup of a high speed liquid jet. *ASME Journal of Fluids Engineering*, submitted, 2010.

[7] W. Bo, X. Liu, J. Glimm, and X. Li. A robust front tracking method: Verification and application to simulation of the primary breakup of a liquid jet. *SIAM J. Sci. Comput.*, submitted, 2010.

[8] Wurigen Bo. Applications of 3d front tracking to multi phase fluid. *Ph.D thesis, Applied Mathematics and Statistics Department, Stony Brook University*, 2009.

[9] S. Chandrasekhar. *Hydrodynamic and Hydromagnetic Stability*. Oxford University Press, Oxford, 1961.

[10] O. Desjardins, V. Moureau, and H. Pitsch. An accurate conservative level set/ghost fluid method for simulating turbulent atomization. *J. Comput. Phys.*, 227:8395–8416, September 2008.

[11] Jian Du, Brian Fix, James Glimm, Xicheng Jia, Xiaolin Li, Yunhua Li, and Lingling Wu. A simple package for front tracking. *J. Comput. Phys.*, 213:613–628, 2006.

[12] C. Dumouchel. On the experimental investigation on primary atomization of liquid streams. *Experiments in Fluids*, 45:371–422, September 2008.

[13] J. Glimm, M. J. Graham, J. W. Grove, X.-L. Li, T. M. Smith, D. Tan, F. Tangerman, and Q. Zhang. Front tracking in two and three dimensions. *Comput. Math. Appl.*, 35(7):1–11, 1998.

[14] J. Glimm, J. W. Grove, X.-L. Li, K.-M. Shyue, Q. Zhang, and Y. Zeng. Three dimensional front tracking. *SIAM J. Sci. Comp.*, 19:703–727, 1998.

[15] J. Glimm, J. W. Grove, X.-L. Li, and D. C. Tan. Robust computational algorithms for dynamic interface tracking in three dimensions. *SIAM J. Sci. Comp.*, 21:2240–2256, 2000.

[16] J. Glimm, J. W. Grove, X.-L. Li, and N. Zhao. Simple front tracking. In G.-Q. Chen and E. DiBenedetto, editors, *Contemporary Mathematics*, volume 238, pages 133–149. Amer. Math. Soc., Providence, RI, 1999.

[17] J. Glimm, J. W. Grove, W. B. Lindquist, O. McBryan, and G. Tryggvason. The bifurcation of tracked scalar waves. *SIAM journal on scientific computing*, 9:61–79, 1988.

[18] J. Glimm, E. Isaacson, D. Marchesin, and O. McBryan. Front tracking for hyperbolic systems. *Adv. Appl. Math.*, 2:91–119, 1981.

[19] M. Herrmann. A eulerian level set/vortex sheet method for two-phase interface dynamics. *J. Comput. Phys.*, 203(2):539–571, 2005.

[20] M. Herrmann. On simulating primary atomization using the refined level set grid method. In *Proceedings of ILASS-Americas 21th. annual Conference on Liquid Atomization and Spray*, 2008.

[21] K. Heukelbach and C. Tropea. Influence of the inner flowfielf of flat fan pressure atomizers on the disintegration ofthe liquid sheet. In *17th Annual Conference on Liquid Atomization and Spray Systems*, page 613618, 2001.

[22] H.Hiroyasu, M. Arai, and M. Shimizu. *"Effect of flow conditions inside injector nozzles on jet breakup processes", Recent advances in spray conmbustion: Spray atomization and drop burning phenomena, Volume 1.* American Institute of Aeronautics and Astronautics Inc., 1996.

[23] T. Y. Hou, J. S. Lowengrub, and M. J. Shelley. The long-time motion of vortex sheets with surface tension. *Phys. Fluids*, 9(7):1933–1954, 1997.

[24] Julian Scott Jean Mathieu. *An Introduction to Turbulent Flow.* Cambridge University Press, 2000.

[25] X. Jiao and H. Zha. Consistent computation of first- and second-order differential quantities for surface meshes. In *Proceedings of the ACM Solid and Physical Modeling Symposium*, pages 159–170, 2008.

[26] M. Klein, A. Sadiki, and J. Janicka. A digital filter based generation of inflow data for spatially developing direct numerical or large eddy simulations. *J. Comput. Phys.*, 186:652–665, April 2003.

[27] A. Lefebvre. *Atomization and Sprays.* Hemisphere Publishing Corp., New York, 1989.

[28] V. G. Levich. *Physicochemical Hydrodynamics.* Prentice-Hall, New Jersey, 1962.

[29] X.-L. Li, B. X. Jin, and J. Glimm. Numerical study for the three dimensional Rayleigh-Taylor instability using the TVD/AC scheme and parallel computation. *J. Comput. Phys.*, 126:343–355, 1996.

[30] H. Lim, J. Iwerks, J. Glimm, and D. H. Sharp. Nonideal Rayleigh-Taylor mixing. *PNAS*, 2010. In press. Stony Brook Preprint SUNYSB-AMS-09-05 and Los Alamos National Laboratory preprint number LA-UR 09-06333.

[31] H. Lim, Y. Yu, J. Glimm, X. L. Li, and D. H. Sharp. Subgrid models for mass and thermal diffusion in turbulent mixing. *Physica Scripta*, 2009. Stony Brook Preprint SUNYSB-AMS-08-07 and Los Alamos National Laboratory Preprint LA-UR 08-07725; Submitted for Publication.

[32] S. P. Lin and R. D. Reitz. Drop and spray formation from a liquid jet. *Annu. Rev. Fluid Mech.*, 30:85–105, 1998.

[33] Mark Linne, Megan Paciaroni, Tyler Hall, and Terry Parker. Ballistic imaging of the near field in a diesel spray. *Experiments in Fluids*, 40(6):836–846, June 2006.

[34] J.-J. Liu, J. Glimm, and X.-L. Li. A conservative front tracking method. In F. Asakura, H. Aiso, S. Kawashima, Matsumura A, S. Nishibata, and K. Nishihara, editors, *Hyperbolic Problems: Theory, Numerics, and Applications*, pages 57–62. Yokohama Publishers, Osaka, Japan, 2006.

[35] X. F. Liu, E. George, W. Bo, and J. Glimm. Turbulent mixing with physical mass diffusion. *Phys. Rev. E*, 73:056301, 2006.

[36] X. F. Liu, Y. H. Li, J. Glimm, and X. L. Li. A front tracking algorithm for limited mass diffusion. *J. of Comp. Phys.*, 222:644–653, 2007. Stony Brook University preprint number SUNYSB-AMS-06-01.

[37] Xingtao Liu. Comparison between adding 2D cylindrical coordinate source term. http://www.ams.sunysb.edu/ liuxt12/research/2dsrc.

[38] Andrew G. MacPhee, Mark W. Tate, and Christopher F. Powell. X-ray imaging of shock waves generated by high-pressure fuel sprays. *Science*, 295:1261–1263, 2002.

[39] T. Menard, S. Tanguy, and A. Berlemont. Coupling level set/VOF/ghost fluid methods: Validation and application to 3D simulation of the primary break-up of a liquid jet. *International Journal of Multiphase Flow*, 33:510–524, May 2007.

[40] R. Menikoff and B. Plohr. The Riemann problem for fluid flow of real materials. *Rev. Mod. Phys.*, 61:75–130, 1989.

[41] P. Moin, K. Squires, W. Cabot, and S. Lee. A dynamic subgrid-scale model for compressible turbulence and scalar transport. *Phys. Fluids*, A3:2746–2757, 1991.

[42] T. E. Parker and L. R. Rainaldi. A comparative study of room-temperature and combusting fuel sprays near the injector tip using infrared laser diagnostics. *Atomization Spray*, 8:565–600, 1998.

[43] B. Plohr, J. Glimm, and O. McBryan. Applications of front tracking to two-dimensional gas dynamics calculations. In J. Chandra and J. Flaherty, editors, *Computational Aspects of Penetration Mechanics*, volume 3 of *Lect. Notes in Engrg.*, pages 180–191. Springer-Verlag, New York–Heidelberg–Berlin, 1983.

[44] Powel, C. F., Y. Yue, Poola, J. R., Wang, M. Lai, and J. Schaller. Quantitative x-ray measurements of a diesel spray core. In *In Proc. 14th Annual Conference on Liquid Atomization and Spray Systems (ILASS)*, Dearborn, MI, 2001.

[45] L. Rayleigh. On the instability of jets. *Proc. London Math. Soc.*, 10:4–13, 1878.

[46] L. Rayleigh. On the stability of jets. *Proc Lond Math Soc*, 10:4–13, 1878.

[47] R. D. Reitz and F. V. Bracco. On the dependence of spray angle and other spray parameters on nozzle design and operating conditions. In *SAE paper 790494*, 1979.

[48] R. D. Reitz and F. V. Bracco. Mechanism of atomization of a liquid jet. *Phys. Fluids*, 25:1730–1742, 1982.

[49] R. D. Reitz and F. V. Bracco. Mechanisms of breakup of round liquid jets. In *Encyclopedia of Fluid Mechanics*, page 223. Gulf Publishing, 1986.

[50] R.Scardovelli and S.Zaleski. Direct numerical simulaion of free-surface and interfacial flow. *Ann. Rev. Fluid Mech.*, 31:567–603, 1999.

[51] K. A. Sallam and G. M. Faeth. Surface Properties During Primary Breakup of Turbulent Liquid Jets in Still Air. *AIAA Journal*, 41:1514–1524, August 2003.

[52] R. Samulyak, T. Lu, Y. Prykarpatskyy, J. Glimm, Z. Xu, and M. N. Kim. Comparison of heterogeneous and homogenized numerical models of cavitation. *Int. J. Multiscale Comp. Eng.*, 4:377–389, 2006.

[53] J. A. Sethian. *Level Set Methods*. Cambridge University Press, 1996.

[54] H. C. Simmons. *The Correlation of Drop-Size. Distributions in Fuel Nozzle Sprays*, volume 99. 1977.

[55] M. Sterling and C. A. Sleicher. The instability of capillary jets. *Journal of Fluid Mechanics*, 68:477–495, 1975.

[56] W. Tauber, S. O. Unverdi, and G. Tryggvason. The nonlinear behavior of a sheared immiscible fluid interface. *Phys. Fluids*, 14:2871–2885, 2002.

[57] H. Terashima and G. Tryggvason. A front-tracking/ghost-fluid method for fluid interface in compressible flows. *J. Comput. Phys.*, 228:4012–4037, 2009.

[58] G. Tryggvason, B. Bunner, A. Esmaeeli, D. Juric, N. Al-Rawahi, W. Tauber, J. Han, S. Nas, and Y.-J. Jan. A front-tracking method for the computations of multiphase flow. *J. Comput. Phys.*, 169:708–759, 2001.

[59] C. Weber. Disintegration of liquid jets. *Z. Angrew. Math. Mech.*, 11, 1931.

[60] P.R. Williams and R.L. Williams. Measurements of the cavitation threshold of multigrade engine oils under dynamic stressing by pulses of negative pressure. *Professional Engineering Publishing*, 4(4):269–282, 2003.

[61] P.-K. Wu and G.M. Faeth. Aerodynamic effects on primary breakup of turbulent liquids. *Atomization and Sprays*, 3:265–289, 1993.

[62] P.-K. Wu, L.-K. Tseng, G. M. Faeth, J. W. Usry, J. F. Meyers, and L. S. Miller, editors. *Primary breakup in gas/liquid mixing layers for turbulent liquids*, January 1992.

[63] Z. Xu, M. Kim, T. Lu, W. Oh, J. Glimm, R. Samulyak, X. Li, and C. Tzanos. Discrete bubble modeling of unsteady cavitating flow. *J. Multiscale Comp. Eng.*, 4:601–616, 2006.

[64] Z. L. Xu, M. Kim, T. Lu, W. Oh, J. Glimm, R. Samulyak, X. L. Li, and C. Tzanos. Discrete bubble modeling of unsteady cavitating flow. *International Journal for Multiscale Computational Engineering*, 4:601–616, 2006.

[65] Sam S. Yoon. Liquid distributions at the liquid core of a turbulent spray. *Phys. of Fluids*, 17:035103–035103–24, 2005.

Appendix A

Curvature and radial source terms in 2D

A.1   Curvature

We choose z-axis as axis of revolution. The standard parametrization of the surface of revolution is given by:

$$S(u,v) = (\varphi(v)\cos u, \varphi(v)\sin u, \psi(v)). \tag{A.1}$$

Here $\varphi(v)$ is the radius, and $\psi(v)$ is the distance to the origin in the z direction. The unit surface normal of a surface of revolution parametrized by (A.1) are given by:

$$U(u,v) = \frac{sign\varphi}{\sqrt{\psi'^2 + \varphi'^2}}(\psi'\cos u, \psi'\sin u, -\varphi'). \tag{A.2}$$

The principal curvatures of a surface of revolution parametrized by (A.1) are given by

$$k_p = \frac{-\psi'}{|\varphi|\sqrt{\varphi'^2 + \psi'^2}}, \tag{A.3}$$

$$k_m = \frac{(sign\varphi)(\varphi''\psi' - \varphi'\psi'')^{3/2}}{\varphi'^2 + \psi'^2}. \tag{A.4}$$

Here k_p is the curvature of the parallel, and k_m is the curvature of the meridian. Since we are in a 2D cylindrical coordinate system, only k_m and the unit normal at the point can be computed directly. Thus we need to determine k_p. Assume the unit normal at the point is

$$(\cos\theta, \sin\theta)$$

Compare with equation (A.2), we can get

$$\frac{\cos\theta}{\sin\theta} = -\frac{\psi'}{\varphi'}. \tag{A.5}$$

44

This is substituted to (A.3), yielding

$$k_p = \frac{\cos \theta}{\varphi}.$$

$$(A.6)$$

A.2 Radial source terms for the point propagation

As mentioned earlier, we use strang splitting method to solve the Euler equation. If we project the Euler equation in the normal direction, we get

$$\frac{\partial \rho}{\partial t} + v_N \frac{\partial \rho}{\partial N} + \rho \frac{\partial v_N}{\partial N} + \frac{\alpha N_0}{r} \rho v_N = 0,$$

$$(A.7)$$

where ρ is the density, N denotes the normal direction, and N_0 denotes the first component of normal direction. Consider the following normal differential equation:

$$\frac{\partial \rho}{\partial t} = -\frac{\alpha N_0 v_N}{r} \rho.$$

$$(A.8)$$

Since this is a normal projection,

$$dr = v_N N_0 dt.$$

In 2D cylindrical coordinate system, $\alpha = 1$, so

$$\frac{\partial r}{\partial t} = v_N N_0.$$

Substitute this into (A.8) to obtain

$$r \frac{\partial \rho}{\partial t} + \rho \frac{\partial r}{\partial t} = 0,$$

That is,

$$\frac{\partial r \rho}{\partial t} = 0.$$

$$(A.9)$$

A.2.1 Analytic solution

In *FronTier* source code, analytic solution is implemented as

$$\rho = \rho_0 \frac{r0}{r1}$$

which is consistent with (A.9).

45

A.2.2 Modified Euler

The modified Euler method starts with an Euler step, giving a provisional value for w_{i+1} at the next time t_{i+1}:

$$w_{i+1} = w_i + hf(t_i, w_i).$$

The step actually taken looks like an Euler step, but with f replaced by the average of f at the starting point of the step and f at the provisional point:

$$w_{i+1} = w_i + \frac{h}{2} \left[f(t_i, w_i) + f(t_{i+1}, w'_{i+1}) \right]$$

The modified Euler method here is actually a midpoint method of second order.

A.2.3 Backward Euler

From

$$\frac{\partial p}{\partial t} = \frac{\partial p}{\partial \rho} \frac{\partial \rho}{\partial t}$$

we get a nonlinear equation

$$\frac{\partial p}{\partial t} = -\frac{\alpha N_0 v_N}{r} \rho c^2. \tag{A.10}$$

Here c^2 is the function of p and ρ. The backward Euler method is implemented together with a fixed point iteration. This method is first order, but it is stable. If the iteration is not convergent, then after certain number of iterations (typically 20) it may lead to a very bad state. We choose the Modified Euler method or analytic solution instead if it is not convergent.

A.3 Source term for the interior sweep

In *FronTier*, The states in the fluid are solved by conservation laws. The basic variables are density, momentum and total energy. The conservation laws for these variables can be written as

$$\mathbf{U}_t + \nabla \cdot \mathbf{F}(\mathbf{U}) = \mathbf{S} . \tag{A.11}$$

where

$$\mathbf{U} = \begin{pmatrix} \rho \\ \rho \mathbf{v} \\ \rho E \end{pmatrix} \quad \mathbf{F}(\mathbf{U}) = \begin{pmatrix} \rho \mathbf{v} \\ \rho \mathbf{v} \mathbf{v} + p \mathbf{I} \\ \rho E + p \mathbf{v} \end{pmatrix} , \tag{A.12}$$

are the conservative variables and their corresponding flux. ρ, the density, $\mathbf{v}$, the velocity, $E = e + \mathbf{v} \cdot \mathbf{v}/2$, the specific total energy, e, the specific internal energy. p, the pressure, $\mathbf{I}$, an identity matrix. $\mathbf{S}$ represents the source terms for the equations

which are used to model many physical effects such viscosity, gravity, mass diffusion and heat transfer.

In *FronTier*, $\rho, \rho u, E$ are used as basic thermodynamic variable, so the equation will be a little different form:

$$\mathbf{U} = \begin{pmatrix} \rho \\ \rho\mathbf{v} \\ E \end{pmatrix} \quad \mathbf{F(U)} = \begin{pmatrix} \rho\mathbf{v} \\ \rho\mathbf{v}\mathbf{v} + p\mathbf{I} \\ (E + p)\mathbf{v} \end{pmatrix}, \tag{A.13}$$

Consider

$$\rho_t + (\rho u)_x = 0, \tag{A.14}$$

$$\rho_t + \frac{(r\rho u)_r}{r} = 0, \tag{A.15}$$

$$\rho_t + (\rho u)_r = -\frac{\rho u}{r}. \tag{A.16}$$

If we use Lax-Friedrich's method (LF) to discretize this equation, we get the following separately:

$$\rho_i^{n+1} = \frac{\rho_{i+1}^n + \rho_{i-1}^n}{2} - \frac{dt}{2dx}((\rho u)_{i+1} - (\rho u)_{i-1}) \tag{A.17}$$

$$\rho_i^{n+1} = \frac{\rho_{i+1}^n + \rho_{i-1}^n}{2} - \frac{dt}{2dr}((\rho u)_{i+1} - (\rho u)_{i-1}) - dt\frac{(\rho u)_{i+1} + (\rho u)_{i-1}}{2r} \tag{A.18}$$

$$\rho_i^{n+1} = \frac{\rho_{i+1}^n + \rho_{i-1}^n}{2} - \frac{dt}{2dr}((\rho u)_{i+1} - (\rho u)_{i-1}) - dt\frac{(\rho u)_i}{r} \tag{A.19}$$

For high order schemes like VM or TVD, we discretize $(\rho u)_r$ using flux, i.e.

$$\rho_i^{n+1} = \frac{\rho_{i+1}^n + \rho_{i-1}^n}{2} - \frac{dt}{2dr}((\rho u)_{i+1/2} - (\rho u)_{i-1/2}) - dt\frac{(\rho u)_{i+1/2} + (\rho u)_{i-1/2}}{2r}$$

We adapt a similar discretization for momentum and energy equations at a half cell location.

For comparison, please check movies at [37].

Appendix B

AMR and its implementation in *FronTier*

B.1 Introduction

For well behaved problems, a grid of uniform mesh spacing (in each of the coordinate directions) gives satisfactory results. However, there are classes of problems for which the solution is more difficult to estimate in some regions (perhaps due to discontinuities, steep gradients, shocks, etc.) than in others. One could use a uniform grid having a spacing fine enough so that the local errors estimated in these difficult regions are acceptable. But this approach is computationally extremely costly. Besides, for time dependent problems it is difficult to predict in advance a mesh spacing that will give acceptable results.

Adaptive mesh refinement (AMR) is a computational technique for improving the efficiency of numerical simulations of systems of partial differential equations. The basic idea is to refine, both in space and in time, regions of the computational domain in which high resolution is needed to resolve developing features, while leaving less interesting parts of the domain at lower resolutions. In *FronTier* , the physical tracking interface is always a point of interest, which requires high resolution. For the high speed jet problem, the nozzle wall, where the boundary layer effect plays an important role, also requires high resolution.

In AMR we start with a base coarse grid. As the solution proceeds we identify the regions requiring more resolution determined by some parameter characterizing the solution, for example, the region where density or pressure changes dramatically across neighboring cells. The criteria for increased resolution is called an error function. We superimpose finer sub-grids only on these regions. Finer and finer sub-grids are added recursively until either a given maximum level of refinement is reached or the local error has dropped below the desired level. Thus in an adaptive mesh refinement computation grid spacing is fixed for the base grid only and is determined locally for the sub-grids according to the requirements of the problem.

In *FronTier*, the base coarse grid covers the whole computational domain, and the finer grid is overlapped on the coarse one. In each grid patch, the interface and the solution are advanced in time. Then a correction procedure is implemented to

correct the result of interface propagation by communication between patches. The solution states on cell center are also updated in this way.

In practice of front tracking simulations, the simulation with AMR can run at least 4 times faster than for uniform grid with same resolution in finest level.

B.2   Time step in *FronTier* with AMR

The evolution of the solution in time with AMR is more complicated than for a regular time step in *FronTier* . AMR has multiple patches in one processor while the regular time step has only one for each processor. The main steps for propagation with AMR can be summarized as follows:

1. Initial mesh refinement.

2. Interface propagation.

   Normal propagation for each patch

   Interface reconstruction

   Tangential propagation for each patch

3. Interior states update for each patch.

4. If (step % 5 == 0) do regridding

This looks quite similar to regular steps in *FronTier* except that one must handle multiple patches. The initial mesh refinement step and regridding step are similar, which can be summarized as following:

1. Gather information to create the error function.

2. Call external library with the error function as input and get a set of new patches information (for example, size, locate, mesh level, etc.).

3. Transform old states from old patches to new patches.

4. Calculate the computing load in each patch and calculate optimal patch distribution on the whole computing processors. Here the base coarse patch is not counted.

5. Send the finer patches to the right processor.

B.3 Improvement of AMR

Currently working AMR code in *FronTier* is transplanted from Zhiliang Xu's version with some improvements. For example, restructure of AMR makes it possible to to support multiple external AMR library [5]; more complicated cases are handled when interface needs to be cut or merged; more complicated cases are handled when a vapor bubble intersects with the jet interface, etc. In the last case, we need to "open bubbles" as a result of intersection, and use a special type of equation of state called multiple component polytropic gas. These improvements can handle properly for up to four or five levels of mesh refinements. A illustration of AMR meshes can be found in the Figure B.1 and B.2.

FronTier is using Overture as external library to generate mesh hierarchy including the initial mesh refinement and the regridding step. All the advancing and communication step between patches are handled inside *FronTier* . There are some shortcoming of this approach:

- Overture is not actively maintained. For quite a while in the past three years, AMR in *FronTier* was not available due to an old Overture library which doesn't work after a system upgrade in galaxy super-computing system. We made a lot of effort to recompile Overture source code in the new system and make it compatible with new *FronTier* .

- Overture does not support Bluegene so far. Galaxy or Seawolf has very limited computing resources (only hundreds of nodes), while Bluegene has 18 racks IBM Blue Gene/L (a total of 18432 nodes) and 2 racks of Blue Gene/P (a total of 2048 nodes). Unfortunately, we can not utilize this powerful computing resource because Overture depends on some library that Bluegene system does not support. That is part of the reason why we want to work on SAMRAI as an AMR library.

- Insufficiency in mesh generation. Although *FronTier* with AMR can run parallelly, the mesh generation part is not actually paralleled. Each processor runs a copy of Overture to create meshes based on the information only in that computational domain, which apparently decreases the efficiency.

- Insufficiency in communication. After patches are created, we need to compute how to balance them and sent them to the right computing processor. These communications are actually very heavy because we need to send the front information (interface and front states) and interior states information. This restricts the frequency of regridding step while we hope to regrid the whole interface as much as possible to create more adaptive meshes. As a result of balancing between communication cost and eagerness of regridding, we typically do regridding every 5 time steps.

Accordingly, several aspects can be improved to achieve better result, which can be summarized as following:

- Use better mesh generation frame work and make the mesh generation parallel. SAMRAI or CHOMBO, for example.

- Improve communication efficiency between patches. We need a better balancing function which works well with mesh generation to minimize the cost of information communication.
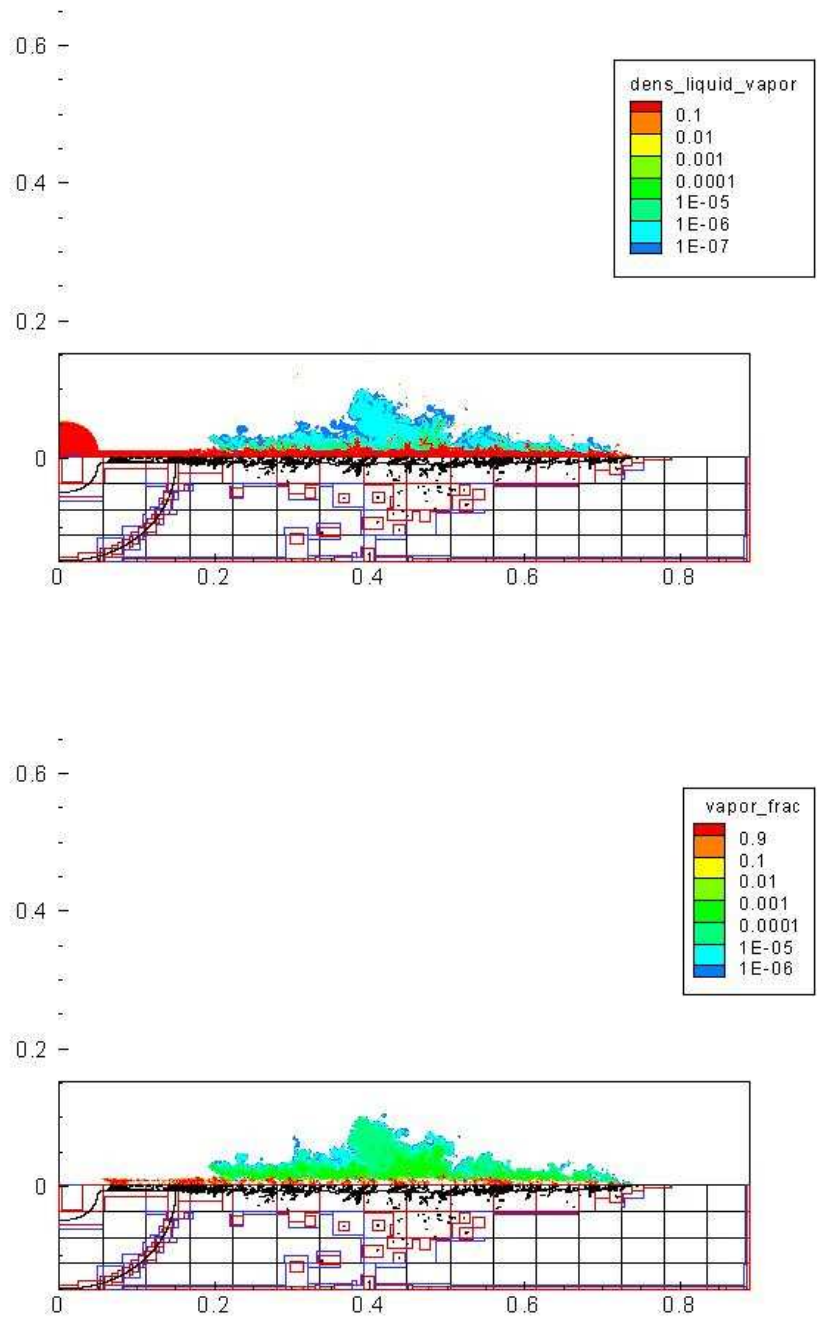
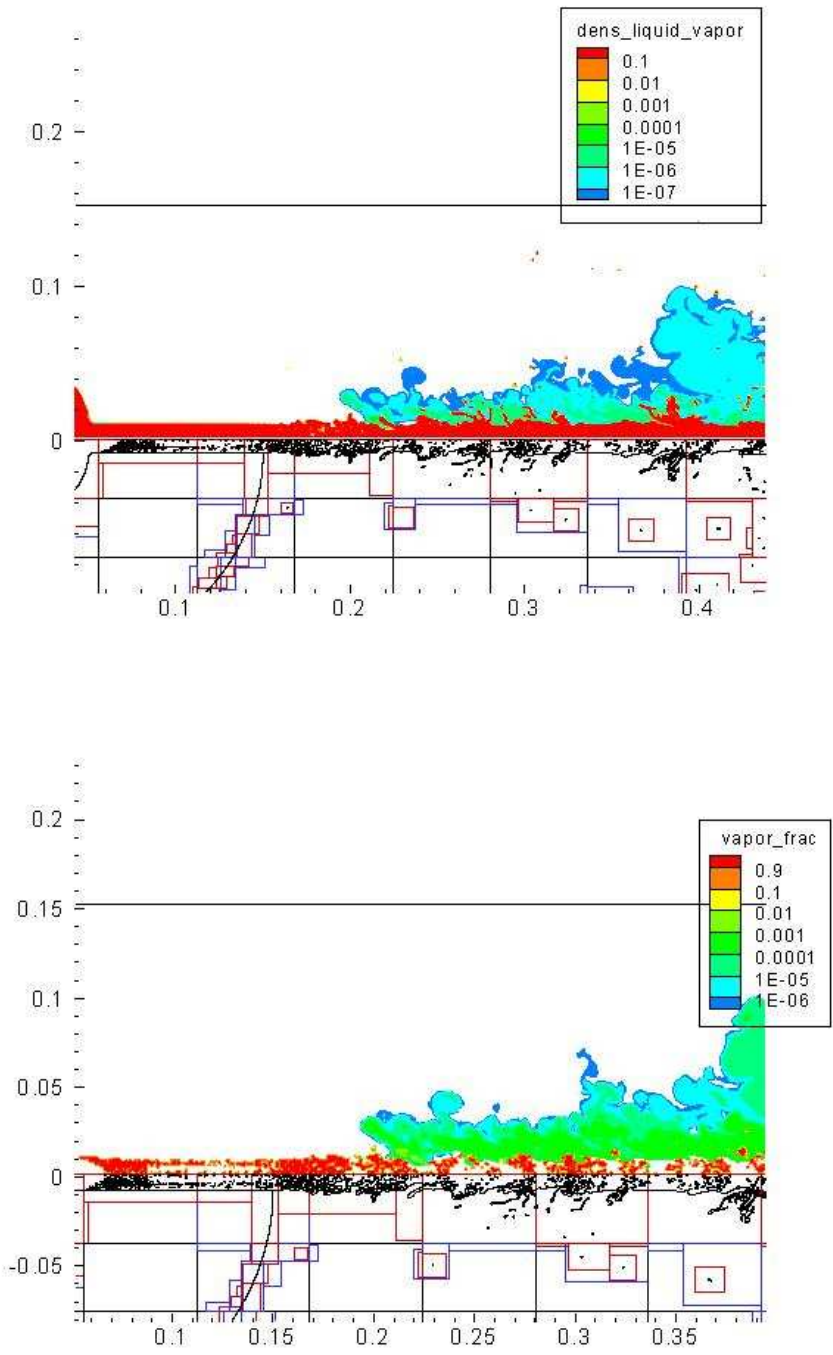Figure B.1: Jet simulation with AMR, density distribution with mesh hierarchy.

Figure B.2: Jet simulation with AMR, vapor fraction distribution with mesh hierarchy.

Appendix C

The importance of a cavitation model

Fig. C.1 shows the interface and pressure contours for the base case and the case with no cavitation model. Both cases show breakup, but there are differences. For the case with no cavitation model, (lower frame), there are three pressure waves inside nozzle, with unphysical pressure minimal as low as -400 bar. When these pressure waves flow out of nozzle, the liquid core breaks immediately into large pieces, and secondary breakup gives small ligaments and drops. For the base case, (upper frame), no such strong pressure waves are formed, as the compressibility of the bubbles mitigates the transient pulses which would otherwise yield strong pressure fluctuations. Once the pressure falls below a critical pressure, a vapor bubble is inserted, and thereby the pressure wave is suppressed. The breakup of the base case is due to turbulent fluctuations within the jet, yielding surface instabilities that grow dynamically, reinforced by interactions between the vapor bubbles and the liquid core surface.
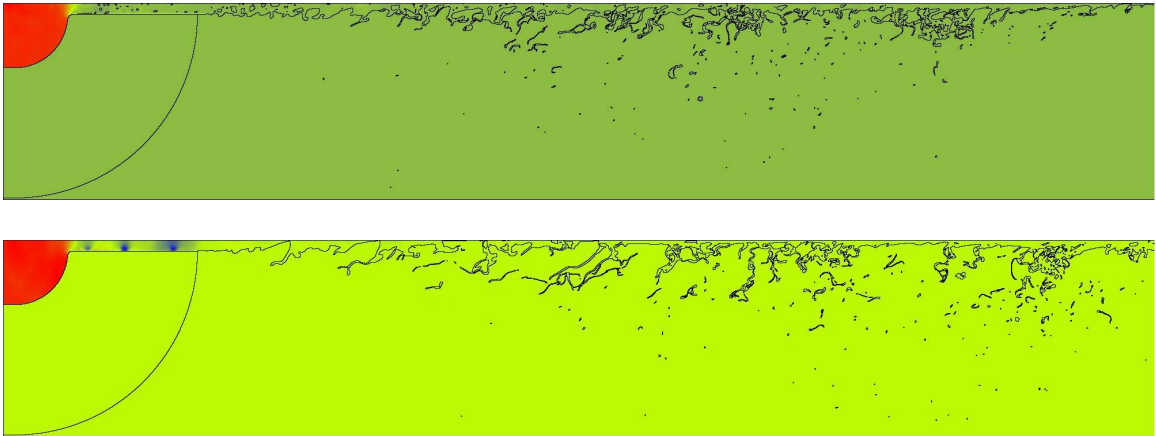

Figure C.1: Late time interface and pressure contour plot, showing jet breakup. Comparison of the simulation with cavitation model (above) to one without it (below).

Appendix D

Additional application for AMR

There are also other interesting problems that can be studied using FrinTier with AMR. We have some preliminary result in following problems:

- Simulation based on real engine geometry. A preliminary result is shown in Figure D.1.

- Cross flow(Hydrogen or Liquid Jet). The preliminary results for both cases are shown in Figure D.2.
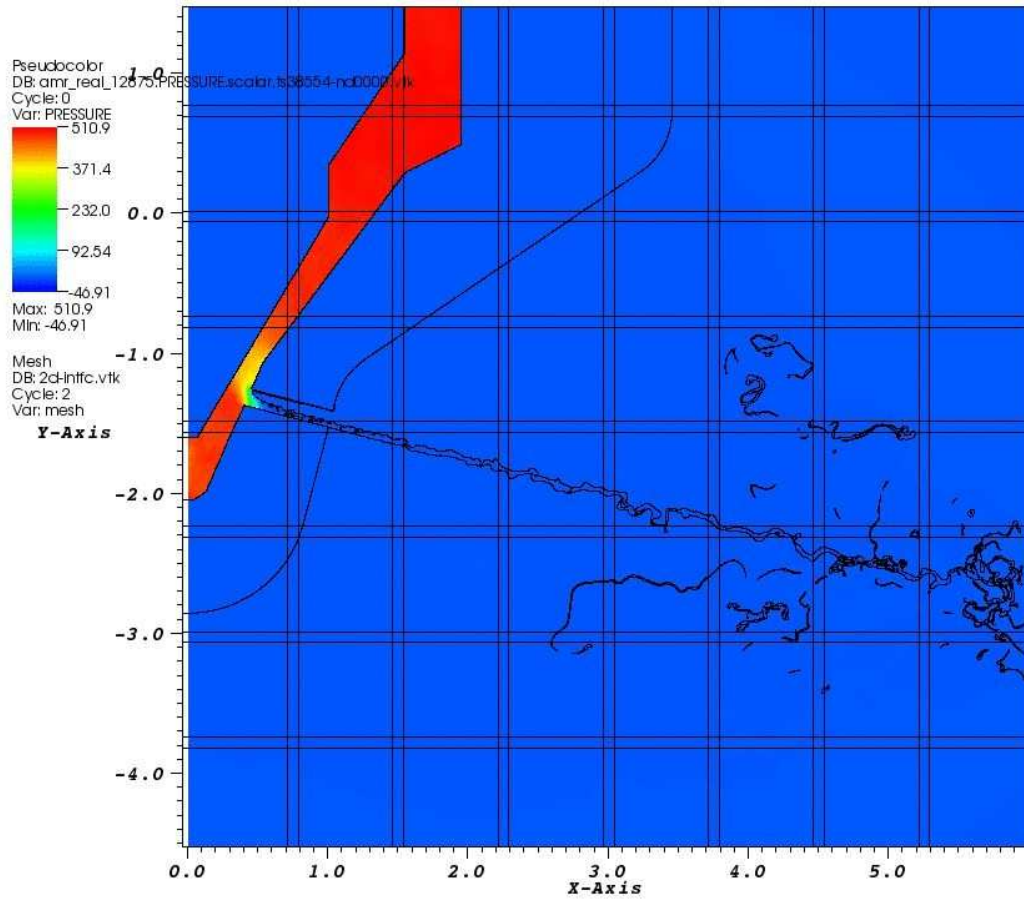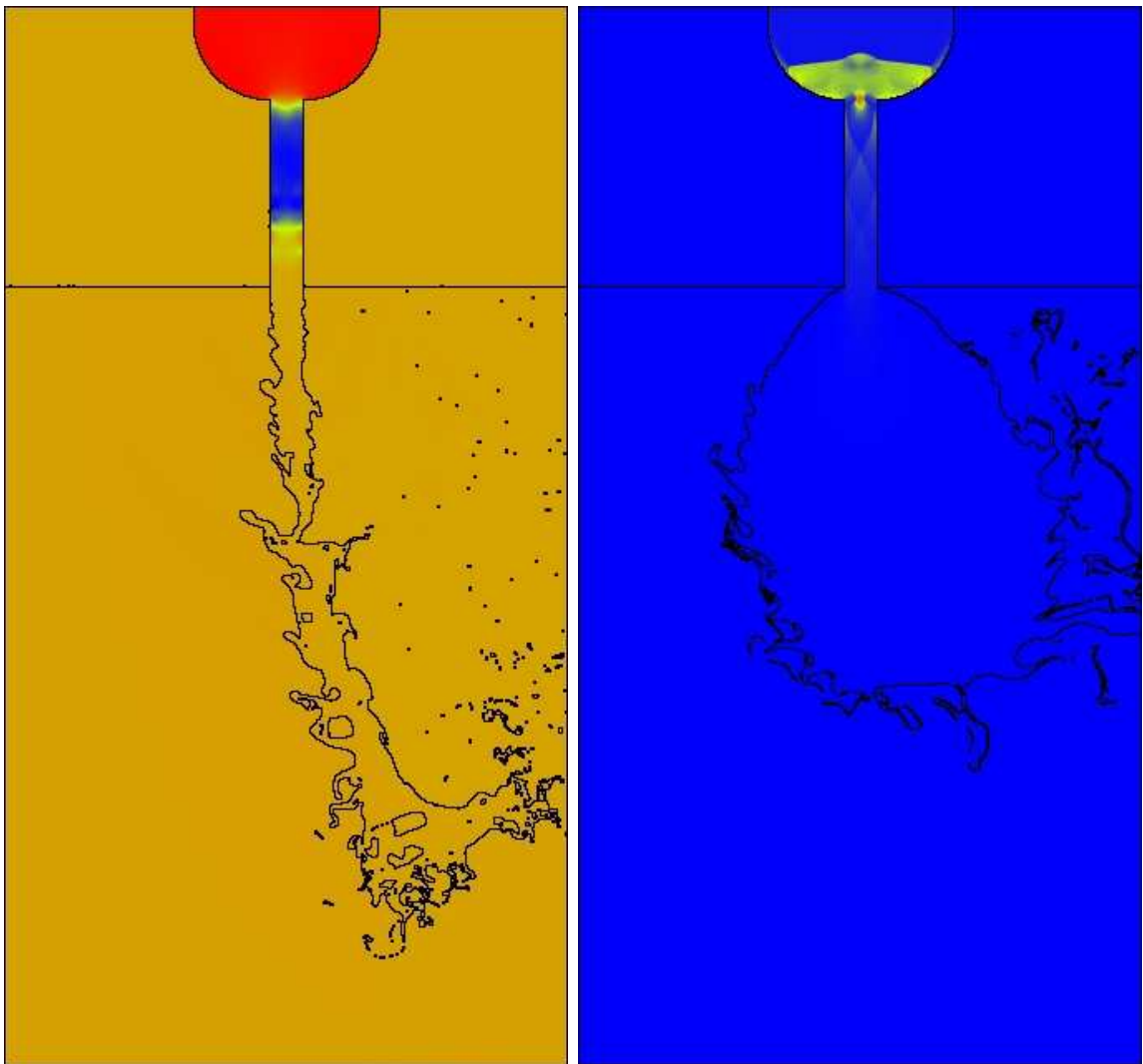
Figure D.1: High speed jet breakup based on real engine geometry

Figure D.2: Cross flow with AMR, Left: N-Heptane, Right: Hydrogen